arXiv:cond-mat/0310768v1 [cond-mat.mtrl-sci] 31 Oct 2003

Model for Spreading of Liquid Monolayers

M. N. Popescu* and S. Dietrich†
Max-Planck-Institut für Metallforschung, Heisenbergstr. 3, D-70569 Stuttgart, Germany, and
Institut für Theoretische und Angewandte Physik,
Universität Stuttgart, Pfaffenwaldring 57, D-70569 Stuttgart, Germany
(Dated: February 2, 2008)

Manipulating fluids at the nanoscale within networks of channels or chemical lanes is a crucial challenge in developing small scale devices to be used in microreactors or chemical sensors. In this context, ultra-thin (i.e., monolayer) films, experimentally observed in spreading of nano-droplets or upon extraction from reservoirs in capillary rise geometries, represent an extreme limit which is of physical and technological relevance since the dynamics is governed solely by capillary forces. In this work we use kinetic Monte Carlo (KMC) simulations to analyze in detail a simple, but realistic model proposed by Burlatsky *et al.* [1, 2] for the two-dimensional spreading on homogeneous substrates of a fluid monolayer which is extracted from a reservoir. Our simulations confirm the previously predicted time-dependence of the spreading, $X(t \to \infty) = A\sqrt{t}$, with $X(t)$ as the average position of the advancing edge at time t, and they reveal a non-trivial dependence of the prefactor A on the strength U_0 of inter-particle attraction and on the fluid density C_0 at the reservoir as well as an U_0-dependent spatial structure of the density profile of the monolayer. The asymptotic density profile at long time and large spatial scale is carefully analyzed within the continuum limit. We show that including the effect of correlations in an effective manner into the standard mean-field description leads to predictions both for the value of the threshold interaction above which phase segregation occurs and for the density profiles in excellent agreement with KMC simulations results.

PACS numbers: 68.15.+e, 68.37.-d, 81.15.Aa

I. INTRODUCTION

In the context of microfluidics, wetting phenomena at the micro- and nano-meter scale [3, 4, 5, 6, 7] are relevant for applications like microreactors or chemical sensors, for which a crucial challenge is the transport of liquid to networks of channels or chemical lanes, as well as its precise manipulation within such a network [8, 9, 10]. Since at this small scale the liquid-substrate interaction is important, the flow of thin films may be eventually controlled by engineering the physico-chemical properties of the substrate, thus opening the road for applications which do not have an equivalent at the macroscopic scale [11, 12, 13].

Although the existence of very thin precursor films has been long ago evidenced by the studies of Hardy [14], only recent experiments on liquid spreading on atomically smooth surfaces [15, 16, 17, 18, 19, 20, 21, 22], performed with volumes of the order of nano-liters, have clearly shown by means of dynamic ellipsometry or X-ray reflectivity measurements that one or few precursor films with *molecular thickness* and *macroscopic extent* advance in front of the macroscopic liquid wedge of the spreading drop. The liquids used were low-molecular-mass polymer oils which behave as non-volatile liquids, and experiments performed both for spreading of nano-droplets and for capillary rise geometries have established that the linear extent $X(t)$ of the precursor film grows in time as $X(t \to \infty) \sim At^{\alpha}$. The exponent $\alpha = 1/2$ seems to be independent of the nature of the liquid and of the substrate, of the geometry, and of the volume of droplet as long as the droplet is not emptied and constitutes a reservoir for the extracting film; only the prefactor A depends on these parameters.

Several theoretical models have been proposed (see Refs. [1, 2, 23, 24, 25, 26] and references therein) and an impressive number of Molecular Dynamics (MD) and Monte Carlo (MC) numerical simulations have been performed (see Refs. [7, 27, 28, 29, 30, 31, 32, 33, 34] and references therein) in order to understand the mechanisms behind the extraction of precursor films and to explain the time dependence of the spreading.

The hydrodynamic model of de Gennes and Cazabat [23] assumes a layered structure of the droplet, each layer being a two-dimensional incompressible fluid, in which vertical transport is possible only at the edges of the layers. The model leads to the correct time dependence for the advancing layers, but, as pointed out in Refs. [1], [24], and [34], it is debatable if this hydrodynamic description holds at the molecular level and can be directly applied to ultra-thin films.

A different approach, along the line of earlier work on activated kinetics by Cherry, Holmes, Blake, and Haynes [35, 36], consists of a microscopic description for the thin liquid films in terms of lattice gas models for interacting particles. One such model is the two-dimensional driven Ising model recently proposed by Abraham *et al.* [26]. Using kinetic Monte Carlo (KMC) simulations it was shown that in this model the transport of mass occurs via a second layer, and a particle-hole diffusion equation was used to show that the model leads to correct predictions

*Electronic address: popescu@mf.mpg.de
†Electronic address: dietrich@mf.mpg.de

(confirmed also by simulations) for the time dependence of spreading. The model predicts a uniform density and a compact first monolayer, in close resemblance of the incompressible layers of the hydrodynamical model mentioned before.

For the case that the precursor consists of a single monolayer, a lattice gas model of interacting particles has been proposed by Burlatsky *et al.* [1]. This model, which allows mass transport from the reservoir to the advancing edge only inside the monolayer, has been extended to the more general situation of relaxation of a monolayer initially occupying a half-plane without a reservoir by Oshanin *et al.* [2]. Based on several mean-field assumptions, among which the strongest is the replacement of the inter-particles attraction in the "bulk" by an "effective force" acting on the advancing edge, the authors have been able to derive the $t^{1/2}$-law for the spreading and to calculate the dependence of the prefactor on the fluid-fluid interaction parameters. In contrast to the other two models, in this case the density in the monolayer depends significantly on the distance from the reservoir. Although it is reasonable to expect that neglecting the attractive particle-particle interactions in the "bulk" should not affect the time dependence $\sim t^{1/2}$, one can expect that the behavior in the presence of attractive interactions is much richer (see, for example, the recent KMC simulations results of Lacasta *et al.* [37] for a closely related one-dimensional model).

All three models mentioned above recover the correct time-dependence of spreading, but it is unlikely that one can discriminate between them via experimental tests based on their predictions for the corresponding prefactors because these include in each case a number of parameters whose connections with experimental quantities are not clear. However, we have already pointed out that these models lead to qualitatively different predictions with respect to the shape of the emerging density profiles (constant in the first two cases, spatially varying in the last) which are, in principle, experimentally accessible.

In this work we analyze in detail the density profiles of this last model. We present results of KMC simulations on a square lattice of a model for spreading of a liquid monolayer closely related to the model in Refs. [1] and [2]. Our choice for KMC simulations of a lattice gas model is motivated by the fact that we are interested in the asymptotic (large spatial and temporal scales) behavior, a regime which as yet cannot be explored using Molecular Dynamics simulations because of extensive computing resources needed to simulate spatially large systems and unreasonable large CPU times required to simulate real times even in the order of μ-seconds. In contrast to the previous work mentioned above, we shall explicitely consider the asymmetry of the jump rates in the bulk, at the expense of being able to measure the prefactor A from the simulations but not to predict it analytically. Our results show a non-trivial dependence of the prefactor A on the strength U_0 of the inter-particle attraction and on the density C_0 at the reservoir. The asymptotic spreading behavior at long time and large spatial scale of the transversally averaged density profile is analyzed within a continuum limit. We show that the model predicts qualitatively different structures for the experimentally accessible density profiles along the spreading direction above and below a threshold value for the ratio between the fluid-fluid interaction and the thermal energy. Including the effect of correlations in an effective manner into the standard mean-field description, we find excellent agreement between the theoretical predictions and the KMC results. We conclude the paper with a summary and discussion of the results.

II. DEFINITION AND DISCUSSION OF THE MODEL

As mentioned in the Introduction, a simple microscopic model for the dynamics of a fluid monolayer in contact with a reservoir was proposed in Refs. [1] and [2]. Although we use here this lattice gas model of interacting particles with only slight modifications, for clarity and further reference we describe, motivate, and comment on the defining rules as follows.

(a) The spreading geometry is rectangular ($x-y$ plane) and the substrate is homogeneous. The half-plane $x<0$ is occupied by a reservoir of particles (three-dimensional bulk liquid) at fixed chemical potential which maintains at its contact line with the substrate, positioned at the line $x=0$, an *average* density C_0 (defined as number of particles per unit length in the transversal y direction). For the case of capillary rise, the reservoir would correspond to the liquid bath and the line $x=0$ to the edge of the macroscopic meniscus. It is assumed that the only role of the reservoir is to maintain C_0 constant, and thus to feed the monolayer which is extracted, but there is no flow of particles from the reservoir to "push" the film. The parameter C_0 is expected to be related to the difference in the free energy per particle ΔF between a fluid particle in bulk liquid, i.e., inside the three-dimensional reservoir, and one on the surface of the substrate at $x=0$, and thus it is a measure of the wettability of the substrate by the liquid [21]. A general, explicit form for the relation between C_0 and ΔF is not available, but for a qualitative picture [1, 21] an argument based on Langmuir-type adsorption may be used to estimate $C_0 \approx \sigma C_{reservoir}[1-\exp(-\beta\Delta F)]$, where σ is the area per adsorption site and $C_{reservoir}$ is the density (number of particles per unit volume) in the reservoir. At time $t=0$, the half-plane $x>0$ is empty.

(b) The substrate-fluid interaction is modeled as a periodic potential forming a lattice of potential wells with coordination number z and lattice constant a. The particle motion proceeds via activated jumps between nearest-neighbor wells; evaporation from the substrate is not allowed. We assume that the dynamics of the activated jumps can be described by the classical reaction-rate the-

ory, i.e., the activation barrier U_A is significantly larger than the thermal energy k_BT, where k_B is the Boltzmann constant and T the temperature, and the coupling to the substrate is large enough such that in crossing the barrier all the kinetic energy of the particle is dissipated [38]. The barrier U_A determines the jumping rate $\Omega = \nu_0 \exp[-U_A/k_BT]$, where ν_0 is an attempt frequency defining the time unit. We note that for a two-dimensional homogeneous, isotropic substrate and a regular (square, triangular, honeycomb, etc.) lattice structure, this jumping rate can be absorbed into the one-particle diffusion coefficient $D_0 = \Omega a^2/4$ on the bare substrate [39]. Therefore, in this case U_A is an irrelevant parameter in the sense that it can be incorporated either into the choice of the unit of time as Ω^{-1} or into that of the unit of length as $\sqrt{D_0/\nu_0}$. For the rest of this work we consider a square lattice ($z = 4$); a qualitatively significant dependence of the results on the lattice type is not expected. This expectation is based on corresponding results obtained from test simulations on a triangular lattice ($z = 3$).

(c) The pair interaction between fluid particles at distance r is taken to be hard-core repulsive at short range, preventing double occupancy of the wells, and attractive at long range, $-U_0/r^6$ for $r \geq 1$, resembling a Lennard-Jones type interaction potential. Here and in the following r is measured in units of a so that U_0 denotes the strength of the interaction energy. The absence of double occupancy leads to an *a priori* removal of thickening of the film as a possible relaxation mechanism, which is not meant to imply that we consider it irrelevant. We have decided to disregard this mechanism here since it would have significantly increased the complexity of the problem. Thus we leave the issue of film thickening open for further research.

(d) As we have mentioned in **(a)**, the motion proceeds via activated jumps between nearest-neighbor wells, the activation barrier for any jump being U_A. The selection of the nearest-neighbor well, i.e., the probability $p(\boldsymbol{r} \to \boldsymbol{r'}; t)$ that a jump from location $\boldsymbol{r}$ will be directed toward the location $\boldsymbol{r'}$, is biased by the fluid-fluid energy landscape and is given by

$$p(\boldsymbol{r} \to \boldsymbol{r'}; t) = \frac{\exp\left\{\frac{\beta}{2}[\tilde{U}(\boldsymbol{r}; t) - \tilde{U}(\boldsymbol{r'}; t)]\right\}}{Z(\boldsymbol{r}; t)}, \qquad (1)$$

where $Z(\boldsymbol{r}; t) = \sum_{\boldsymbol{r'}, |\boldsymbol{r'}-\boldsymbol{r}|=1} \exp\left\{\frac{\beta}{2}[\tilde{U}(\boldsymbol{r}; t) - \tilde{U}(\boldsymbol{r'}; t)]\right\}$ is the normalization constant and $1/\beta = k_BT$,

$$\tilde{U}(\boldsymbol{r}; t) = -U_0 \sum_{\boldsymbol{r'}, 0<|\boldsymbol{r'}-\boldsymbol{r}|\leq 3} \frac{\eta(\boldsymbol{r'}; t)}{|\boldsymbol{r} - \boldsymbol{r'}|^6}, \qquad (2)$$

and $\eta(\boldsymbol{r'}; t) \in \{0, 1\}$ is the occupation number of the well at $\boldsymbol{r'}$ at the time t. We note that, after canceling the common factor $\exp[\beta\tilde{U}(\boldsymbol{r}; t)/2]$, the expression Eq. (1) may be re-written in a form which is somewhat simpler for the numerical simulations,

$$p(\boldsymbol{r} \to \boldsymbol{r'}; t) = \frac{\exp\left[-\frac{\beta}{2}\tilde{U}(\boldsymbol{r'}; t)\right]}{\sum_{\boldsymbol{r'}, |\boldsymbol{r'}-\boldsymbol{r}|=1} \exp\left[-\frac{\beta}{2}\tilde{U}(\boldsymbol{r'}; t)\right]}, \qquad (3)$$

the dependence on $\boldsymbol{r}$ being retained because the summation is carried out over the neighboring locations of $\boldsymbol{r}$. We also note that the summation in Eq. (2) has been restricted to three lattice units for computational convenience. This corresponds to the cut-off generally used in Molecular Dynamics simulations for algebraically decaying Lennard-Jones pair-potentials.

The expression Eq. (1) for the probability that a certain direction is chosen for jumping deserves further discussion. For a particle located at $\boldsymbol{r}$, it follows from the definition of $p(\boldsymbol{r} \to \boldsymbol{r'}; t)$ (Eq. (1)) that the rates

$$\omega_{\boldsymbol{r} \to \boldsymbol{r'}; t} = \Omega p(\boldsymbol{r} \to \boldsymbol{r'}; t) \qquad (4)$$

for the transitions from $\boldsymbol{r}$ to neighboring locations $\boldsymbol{r'}$ satisfy

$$\sum_{\boldsymbol{r'}, |\boldsymbol{r'}-\boldsymbol{r}|=1} \omega_{\boldsymbol{r} \to \boldsymbol{r'}; t} \equiv \Omega. \qquad (5)$$

Thus the total rate of leaving a location for any given particle at any given location is determined only by the fluid-solid interaction characterized by U_A, it is time-independent, and it equals Ω. Therefore, the fluid-fluid interaction will influence *only* the choice of a *direction* for the jump, but not the jumping frequency, and in the dynamics there will be only one relevant microscopic time scale, Ω^{-1}, which is dictated by the solid-fluid coupling.

The choice $p(\boldsymbol{r} \to \boldsymbol{r'}; t) \propto \exp\left\{\frac{\beta}{2}[\tilde{U}(\boldsymbol{r}; t) - \tilde{U}(\boldsymbol{r'}; t)]\right\}$ is motivated by the following. If one disregards the reservoir and considers a system with a given volume and a given number of particles, the change in the total fluid-fluid energy (no double occupancy) $U_t = 1/2 \sum_{\boldsymbol{r}} \eta(\boldsymbol{r}; t)\tilde{U}(\boldsymbol{r}; t)$ due to a change in configuration

$$\{\eta(\boldsymbol{r}) = 1, \eta(\boldsymbol{r'}) = 0\} \to \{\eta(\boldsymbol{r}) = 0, \eta(\boldsymbol{r'}) = 1\}, \qquad (6)$$

where $|\boldsymbol{r} - \boldsymbol{r'}| = 1$, is given by $\Delta U_t = \tilde{U}(\boldsymbol{r'}; t) - \tilde{U}(\boldsymbol{r}; t)$, with $\tilde{U}(\boldsymbol{r'}; t)$ calculated for the final configuration and $\tilde{U}(\boldsymbol{r}; t)$ for the initial one. Then a simple choice of transition rates $\omega'_{\boldsymbol{r} \to \boldsymbol{r'}; t}$ which satisfies detailed balance with respect to the equilibrium distribution

$$\mathcal{P} = \exp(-\beta U_t)/\mathcal{Z}, \qquad (7)$$

where $\mathcal{Z} = \sum_{all\ \{\eta(\boldsymbol{r}; t)\}} \exp(-\beta U_t)$, is

$$\omega'_{\boldsymbol{r} \to \boldsymbol{r'}; t} = \Omega \exp(-\beta \Delta U_t/2). \qquad (8)$$

If the transition rates would be chosen according to the

expression Eq. (8) above, then the fluid-fluid interaction would effectively change the activation barrier and lead to a whole spectrum of microscopic time scales. Normalizing these local transition rates (Eq. (8)) by the (local) total transition rate $\sum_{\boldsymbol{r}',|\boldsymbol{r}'-\boldsymbol{r}|=1} \omega'_{\boldsymbol{r}\to\boldsymbol{r}';t}$, a decoupling results between an activated dynamics determined by the solid-fluid interaction and a weak perturbation due to the fluid-fluid interaction, and the choice given in Eq. (1) for the bias probability $p(\boldsymbol{r}\to\boldsymbol{r}';t)$ is obtained. One should note that this decoupling is obtained at the expense that the transition rates $\omega_{\boldsymbol{r}\to\boldsymbol{r}';t}$ defined by Eq. (4) do not satisfy detailed balance with respect to the distribution in Eq. (7), although the deviations, which are equal to $Z(\boldsymbol{r};t)/Z(\boldsymbol{r}';t)$ due to

$$\frac{\omega_{\boldsymbol{r}\to\boldsymbol{r}';t}}{\omega_{\boldsymbol{r}'\to\boldsymbol{r};t}} = \frac{Z(\boldsymbol{r};t)}{Z(\boldsymbol{r}';t)} \exp(-\beta\Delta U_t), \tag{9}$$

are expected to be very small. From this point of view, the dynamics defined by Eq. (4) is that of an asymmetric exclusion process [40], but with a position- and time-dependent bias.

(e) As defined by the rules **(a)-(d)**, the model corresponds to mass transport from the reservoir into a two-dimensional vacuum so that a phase with very low-density, due to two-dimensional evaporation, will form in front of the advancing monolayer. The emergence of this low-density phase poses problems in that its long time dynamics, which is of ideal gas type, mixes with that of the following-up "compact" film and leads to serious difficulties in defining the advancing edge of the monolayer. This problem has been encountered earlier also in three-dimensional simulations [7, 27, 28, 29, 32, 33] and, in general, it has been overcome by replacing the simple particles by connected chains mimicking polymers. Although this approach is straightforward it is not very appealing, neither from a theoretical point of view (an analytical approach becomes at least cumbersome, if not intractable), nor from a computational one (the memory and CPU requirements for sufficiently long simulation runs for large enough systems are unreasonably high).

Therefore, we have adopted a different approach. We define the advancing edge Γ_t of a monolayer configuration at time t as the set of the most advanced particles in each line $y = const$ for this configuration (see Fig. 1). We eliminate two-dimensional "evaporation" by imposing the following additional constraint: moves from sites $\boldsymbol{r} \in \Gamma_t$ toward sites $\boldsymbol{r}'$ ahead of Γ_t for which $|\tilde{U}(\boldsymbol{r}';t)| < U_c$, where $U_c \geq 0$ is a fixed threshold value, are rejected. This corresponds to requiring a given minimum number of particles in the neighborhood $|\boldsymbol{r}| \leq r_c$ of any of the components of Γ_t. The results presented in this paper correspond to simulations with $U_c = U_0/3^6$, i.e., $r_c = 3$, in other words to the requirement that in the disk $|\boldsymbol{r}''-\boldsymbol{r}'| \leq 3$ centered at $\boldsymbol{r}'$ there is at least one more particle in addition to the one attempting the jump $\boldsymbol{r}\to\boldsymbol{r}'$ (see also, c.f., Fig. 5).

The above constraint is close in spirit to the "effective boundary-tension" idea used in Ref. [2] in which the attractive interactions have been neglected except for particles on the advancing edge for which a *constant* asymmetry in the jumping rates "away" and "toward" the reservoir was imposed. Rule **(e)** provides a simple and convenient way of controlling the rate of two-dimensional evaporation. For example, setting $U_c = 0$ corresponds to fully unconstrained dynamics, while replacing the rejection procedure with an "acceptance rate" will allow for a continuous tuning of the evaporation rate through the acceptance rate. We note that, physically, the model defined by the rules **(a)-(e)** could be used to study also expansion into an already present vapor phase instead of expansion into vacuum. In the presence of a vapor phase there would be an average occupancy of the sites in front of Γ_t, and thus some of the jumps from Γ_t would be rejected due to the hard-core repulsion, which is an effect similar to an acceptance rate as discussed above.

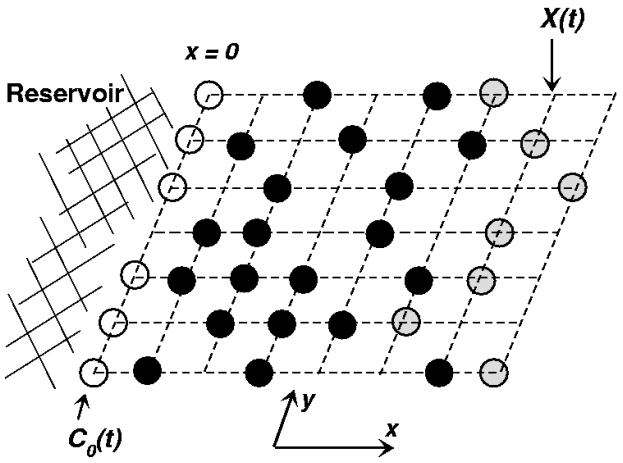

FIG. 1: Schematic drawing of a typical configuration $\{\eta(\boldsymbol{r};t)\}$ of a monolayer spreading on a rectangular lattice (viewed under an oblique angle). The particles denoted as open circles occupy the edge of the reservoir $x = 0$ with $C_0(t)$. Black circles denote the particles in the bulk of the monolayer whereas gray circles denote particles at the advancing edge Γ_t. Also indicated is the average position $X(t)$ of the advancing edge. Here $C_0(t)$ and $X(t)$ correspond to averages over y for a given realization and not to averages over runs (for which we use the same notation in the main text). There are periodic boundary conditions in the $y-$direction.

III. KINETIC MONTE CARLO SIMULATIONS

We have carried out KMC simulations of the model defined in Sect. II using square lattices with widths L_y of 200 or 500 lattice units, periodic boundary conditions along the transversal (y) direction (appropriate for simulating an infinitely wide substrate), and an activation energy $\beta U_A = 3.5$. Some simulation runs have been carried

out using lattices with smaller widths in order to check finite-size effects. We have found that for widths larger than 100 lattice units there is no detectable influence of the width value on the quantities we have measured in these simulations. The length of the lattice in the x direction has been chosen to be $L_x = 1000$ lattice units, with the possibility of changing it dynamically in the course of the simulation if necessary, i.e., if Γ_t intersects the line $x = 1000$; however, this situation was not encountered in any of the simulations we have carried out. We note here that in the experiments mentioned in Sect. I [15, 16, 17, 18, 19, 20, 21] typical values for the diffusion coefficient were estimated from the spreading rate to be of the order of $10^{-11} - 10^{-9}\,\mathrm{m}^2/s$. If we take the lattice spacing as $a \simeq 10\,\mathrm{nm}$, i.e., of the order of the lateral size of a PDMS coil [22], then the above values for the diffusion coefficient imply typical values for the frequency Ω of the order of $10^5 - 10^7\,\mathrm{s}^{-1}$, and thus for $\beta U_A = 3.5$ typical values for ν_0 of the order of $10^6 - 10^8\,\mathrm{s}^{-1}$.

For the simulations we have used a variable step continuous time kinetic Monte Carlo algorithm [41, 42, 43] which is described in Appendix A. One step in the Monte Carlo simulation proceeds as follows. At time t, a particle from the film ($x \geq 0$) is selected at random. The time is incremented with Δt (the time at which a jump attempt with sufficient energy for leaving the well *will occur*), where Δt is a random variable distributed according to $P(\Delta t) = N\Omega \exp(-N\Omega\Delta t)$ [41, 42, 43], and N is the number of particles in the film at time t (so that $\langle \Delta t \rangle_P = \dfrac{1}{N\Omega}$). The direction for the jump is chosen at random with probabilities weighted according to Eq. (1). If the destination site is empty, the jump takes place; if not, the jump is rejected. Exchange between the reservoir ($x < 0$) and film ($x \geq 0$) is subject to the additional constraint that the density $C_0(t) = \dfrac{1}{L_y}\sum_{y=1}^{L_y} \eta(x = 0, y; t)$ on the line $x = 0$ fluctuates narrowly around a given value C_0 and proceeds in the following manner. Moves from $x = 0$ to $x = -1$ are allowed if $C_0(t)$ is maintained within the interval $[C_0(1-\delta), C_0(1+\delta)]$, where the amplitude δ has been fixed to 10^{-2}. If this condition is satisfied, the particle is considered to become part of the reservoir and is removed; if not, the move is rejected. In case of moves from $x = 0$ to $x = 1$, if the density on $x = 0$ would decrease below $C_0(1-\delta)$, then after the move a new particle is added on an empty site (chosen at random) on the line $x = 0$. Similarly, in case of moves from $x = 1$ to $x = 0$ a particle is removed (at random) from the line $x = 0$ if the density would increase above $C_0(1+\delta)$. The time is not incremented upon adding or removing particles, corresponding to the reasonable assumption that the equilibration of the reservoir is very fast. In order to compute the potential energy at a destination site on the line $x = -1$, needed for the evaluation of the weight probabilities for jumping of a particle on the line $x = 0$, in the beginning of the simulation particles are placed at random on the lines $-4 \leq x \leq -1$ such that the average density on these lines is C_0, and this configuration is kept unchanged during the simulation run. Due to these procedures one does not have to consider the dynamics on the lines $x \leq -1$, i.e., in the reservoir. In order to have sufficient fluctuations in $C_0(t)$ on the line $x = 0$, fluctuations which mimic the stochastic nature of the exchange of particles between the reservoir and the film, the width L_y has to be large enough such that the amplitude δ translates into a reasonable number of sites. This is the reason why we have used a large value for the width; for example, at $C_0 = 0.8$ and $L_y = 500$, $\delta = 10^{-2}$ translates into 4 sites.

All the "measured" quantities have been averaged over a number of independent simulation runs ranging from 10 to 50, a value of 50 runs being used in most of the cases. These runs differ from each other both with respect to the initial configuration $\{\eta(x = 0, y; t = 0)\}$ and the subsequent sequence of jumps. The observables of interest are defined below. The density $\rho(\boldsymbol{r}; t)$ is defined as $\rho(\boldsymbol{r}; t) = \langle \eta(\boldsymbol{r}; t) \rangle$, where $\langle \cdots \rangle$ means average over different KMC runs. Due to the symmetry of the model, the density profile $\tilde{\rho}(\boldsymbol{r}; t)$ in the limit of infinitely many runs is independent of y, while in the average over a finite number of runs random, uncorrelated fluctuations (whose amplitude decrease with increasing number of runs) occur along the y direction. These fluctuations are suppressed by measuring the transversally averaged density $C(x,t) = \left\langle \dfrac{1}{L_y}\sum_{y=1}^{L_y} \eta(x, y; t) \right\rangle$, and thus it is expected that $C(x,t) \simeq \tilde{\rho}(\boldsymbol{r}; t)$, with strict equality for infinitely many runs. The average position of the advancing edge of the monolayer is defined as $X(t) = \left\langle \dfrac{1}{L_y}\sum_{\boldsymbol{r}\in\Gamma_t} x \right\rangle$. For the case $U_c = U_0/3^6$ (as used for the actual simulations), two-dimensional evaporation is negligible and $X(t)$ (which we shall also call front line) is a good measure for the actual advancing edge of the monolayer. We note here that in the case when no constraint is imposed to prevent two-dimensional evaporation ($U_c = 0$), the front line may be defined as $X(t) = \langle \hat{x}(t) \rangle$ [44], where $\hat{x}(t)$ is the most advanced line corresponding to a given (smallest measurable) density $\hat{C} = \dfrac{1}{L_y}\sum_{y=1}^{L} \eta(\hat{x}, y; t)$. Alternatively, one may follow the time dependence of the mass of the film [37], or use a percolation type definition for the precursor as the set composed of all the particles which are connected along nearest-neighbor bonds with the reservoir, the boundary of this cluster defining Γ_t [26].

Snapshots of typical density profiles during spreading are shown in Fig. 2 for the cases (a) $W_0 = 1.4$ and (b) $W_0 = 0.8$, where we have introduced the notation

$$W_0 = \beta U_0. \tag{10}$$

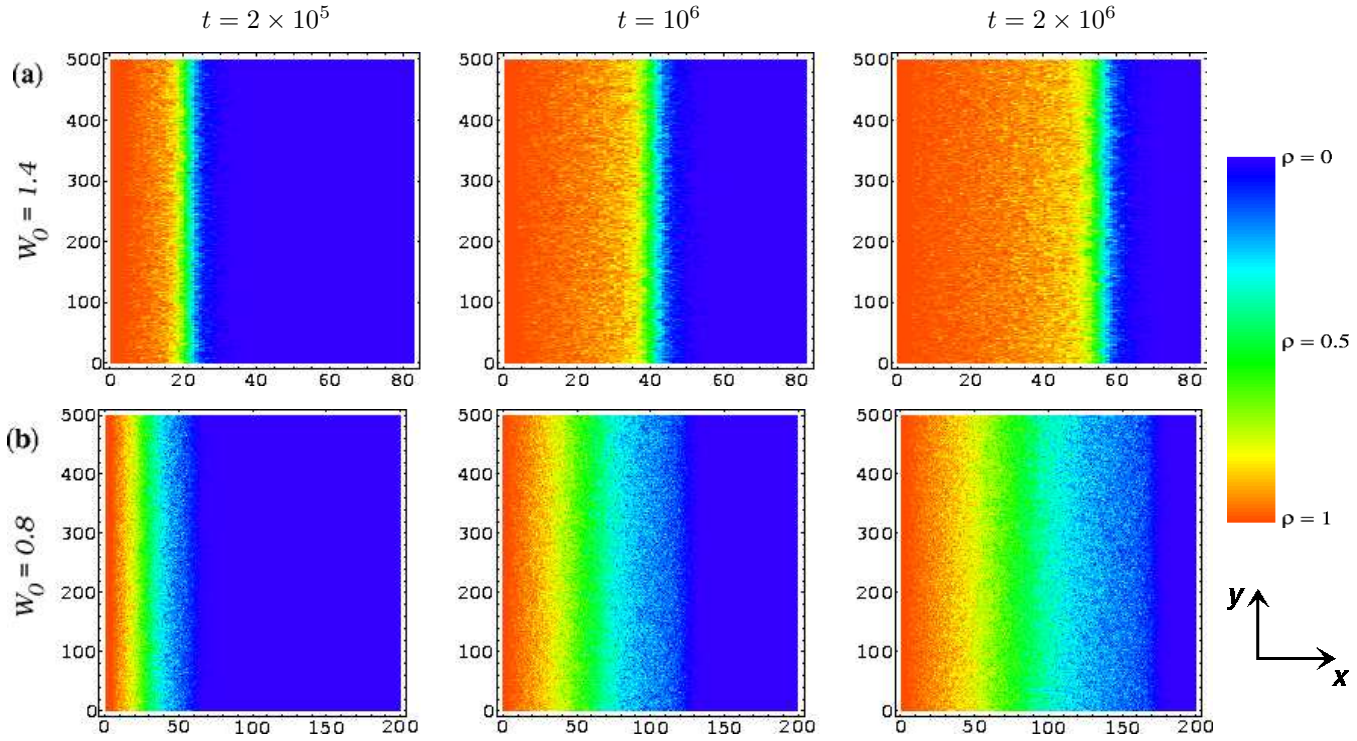

FIG. 2: Typical density profiles $\rho(x, y; t)$ (obtained by averaging over 50 KMC runs) for $W_0 = \beta U_0 = 1.4$ (row (a)) and $W_0 = 0.8$ (row (b)) at times (left to right) $t = 2 \times 10^5$, $t = 10^6$, and $t = 2 \times 10^6$ for $C_0 = 1.0$ and $L_y = 500$. Time is measured in units of $\nu_0^{-1} = \Omega^{-1} \exp(-\beta U_A)$ with $\beta U_A = 3.5$, distances are measured in lattice units, and spreading occurs in $x-$direction. The color coding (shown on the right) is a linear function of density.

These density profiles reveal already the qualitative dynamical behavior. It can be seen that, as expected, the monolayer is homogeneous in the y (transversal) direction, while along the x (spreading) direction there are significant density variations. As intuitively expected, the spreading of the *edge* of the monolayer is faster for smaller W_0, i.e., higher temperature (at a given interaction strength U_0) or smaller inter-particle attraction (at a given temperature T). In addition, one observes qualitatively different dynamics as revealed by the abrupt change from high to low density for the large value of W_0 compared to the smooth and broad decrease for the small value of W_0. This is accompanied by a different dynamics of the regions with moderate to low density in the two cases. While for large value of W_0 (panel (a)) the range of densities $\rho \simeq 0.5$ (the green band) and that of low densities $\rho \lesssim 0.2$ (the light blue band) maintain relatively constant widths and advance with similar rates, for smaller W_0 (panel (b)) the regions become broader with increasing time and clearly the low density (light blue) has a larger rate of advancing. These features will be discussed more in the following sections, where a quantitative characterization of the spreading as a function of the parameters W_0 and C_0 is presented.

IV. TIME-DEPENDENCE OF SPREADING AND ASYMPTOTIC SCALING OF DENSITIES

A. Time dependence of spreading

We start our analysis of the dynamics of spreading by studying the time-dependence of the position $X(t)$ of the front line. As noted in the Introduction, we expect that the asymmetry in the jumping rates due to the inter-particle interactions (Eq. (1)) will not affect the previously (without inter-particle interactions) predicted $X(t) \sim \sqrt{t}$ time dependence as long as the attractive interaction is not too strong. Figure 3 shows the time dependence of the scaled front line, $X(t)/\sqrt{D_0 t}$, for several values of the interaction parameter W_0 and of the reservoir density C_0.

One can see that at low and intermediate values of the interaction strength (Fig. 3(a)) the $\sqrt{t}$ behavior is recovered independent of the value C_0 of the density in the reservoir. However, for strong attractive fluid-fluid interaction (Fig. 3(b)) and low densities C_0, the time dependence of $X(t)$ clearly deviates from the $\sqrt{t}$ behavior, the latter being obtained only for high densities C_0. Since the decreasing trend shown by the data in Fig. 3(b) may be due to either spreading at a rate slower than $\sqrt{t}$, or to the fact that there is no extraction of a macroscopic film from the reservoir, we have also analyzed the time dependence of the total mass of the film extracted,

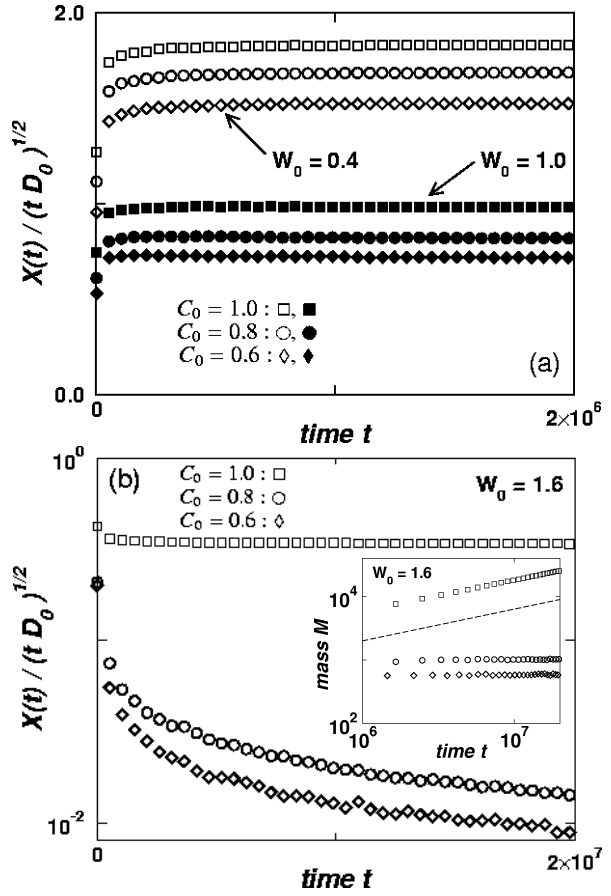

FIG. 3: Front line position (divided by $\sqrt{D_0 t}$) as a function of time for (a) $W_0 = 0.4$ (open symbols) and $W_0 = 1.0$ (filled symbols), and (b) $W_0 = 1.6$, for reservoir densities $C_0 = 1.0$ (squares), $C_0 = 0.8$ (circles), and $C_0 = 0.6$ (diamonds). The inset (on logarithmic scales) compares the time dependence of the (unscaled) mass $M(t)$ of the film for $W_0 = 1.6$ and for the same reservoir densities (symbols) with the $t^{1/2}$ behavior (dashed line). In (b) for $C_0 = 0.8$ and $C_0 = 0.6$ the scaled front line position decays $\sim t^{-1/2}$ for large t. Here and in the following time t is measured in units of $\nu_0^{-1} = \Omega^{-1} \exp(-\beta U_A)$ with $\beta U_A = 3.5$, so that $\sqrt{D_0 t} = \sqrt{\nu_0 t}\ \frac{a}{2}\ \exp(-\frac{1}{2}\beta U_A)$.

$M(t) = \left\langle \sum_{x>0,\,y} \eta(\boldsymbol{r};t) \right\rangle$. As can be seen in the inset in Fig. 3(b), for large C_0 the time dependence of $M(t)$ is very well described by $\sqrt{t}$, as expected [1], while for low values C_0 the mass $M(t)$ shows a clear saturation to a small constant value (which corresponds roughly to a position of the front of ca. 10 lattice units), thus indicating that actually there is no macroscopic film extracted from the reservoir. At early times fluctuations lead to the extraction or leakage (with a very fast decreasing rate of extraction) of a small number of particles from the reservoir, but the spatial extension $X(t)$ of the film in this case remains microscopicly small and becomes time independent for $t \gg 1$. Therefore, as a function of the interaction strength W_0 there is a transition from a "substrate covering" state at low values W_0, in the sense of extraction of a film with macroscopic lateral extension in the spreading direction independently of the density value C_0 in the reservoir edge, i.e., a film which spreads according to $X(t \to \infty) \sim \sqrt{t}$, to a "non-covering" state at large values W_0, in the sense that a macroscopic film is extracted only for sufficiently large densities C_0 (eventually for none if W_0 is sufficiently large). Results similar to the ones shown in Fig. 3, from simulations performed for a broad range of parameters values ($0.4 \le W_0 \le 1.6$ and $0.1 \le C_0 \le 1.0$) indicate that the values $W_0^{(cov)}(C_0)$ for which this change in behavior occurs are bounded from below by $1.0 < W_0^{(cov)}(C_0)$. We shall return to this point in the next but one paragraph and during the discussion of the continuum limit.

The results presented in Fig. 3 also show that in case of spreading the time independent dimensionless prefactor A in $X(t \to \infty) = A\sqrt{D_0 t}$ depends on both W_0 and C_0. From the curves $X(t)/\sqrt{D_0 t}$ one can estimate $A = \lim_{t\to\infty} X(t)/\sqrt{D_0 t}$ by fitting the data in the range $t \gg 1$ (in practice the data in the last tenth of the time interval available) with a constant. The results for $A(C_0, W_0)$ are shown in Fig. 4(a). Here we use the convention that in the case where there is no macroscopic film spreading in the sense explained above, i.e., $X(t)/\sqrt{D_0 t}$ decreases in time and $M(t)$ has a time dependence t^{α_1} with α_1 significantly smaller than 1/2 (in practice $\alpha_1 < 0.4$), the value of the prefactor is assigned to be $A = 0$. As expected, $A(C_0, W_0)$ is an increasing function of C_0 for fixed W_0 and a decreasing function of W_0 for fixed C_0. However, the functional dependence is not simple, and one can easily notice a change in the shape of $A(C_0, W_0)$ for W_0 close to the value 1.0. For values $W_0 \gtrsim 1$, the curve shows a plateau over a range of densities C_0 which increases with increasing W_0, while for values $W_0 \lesssim 1$ the prefactor A is a strictly increasing function of C_0. This property is of a different type than the transition from covering to non-covering discussed above, because it involves a change in the dependence of the prefactor A on the density C_0 while the spreading law $X(t) \sim t^{1/2}$ holds. This change in behavior emerges (as we shall discuss in more detail in the next section) as a consequence of the competition between the diffusive motion driven by the concentration gradient and the clustering tendency (opposing the concentration gradients) driven by the inter-particle attraction. This competition leads to instabilities at certain density values if the attractive interaction is sufficiently strong. From Fig. 4(a), the value of the threshold interaction $W_0^{(t)}$ for the onset of a plateau can be estimated to be bounded as $1.0 < W_0^{(t)} < 1.2$. As shown in the inset, these bounds are confirmed also by the behavior of the derivative $dA(C_0)/dC_0$, which is clearly larger than zero for $W_0 = 1.0$, and becomes zero (within the limits of numerical accuracy) around $C_0 \simeq 0.5$ for $W_0 = 1.2$.

For C_0 fixed the values of the prefactor $A(C_0, W_0)$ as a function of W_0 can be used to estimate via lin-

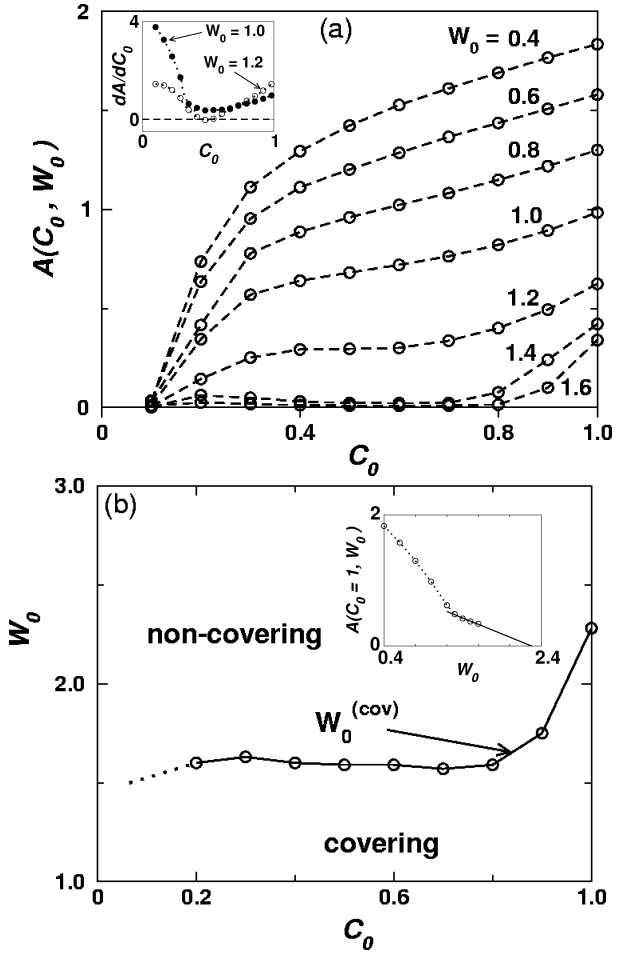

FIG. 4: (a) Dependence of the prefactor $A(C_0, W_0)$ on C_0 for several values of W_0. The inset shows the derivative $dA(C_0)/dC_0$ as a function of C_0 in the cases $W_0 = 1.2$ (○) and $W_0 = 1.0$ (●); the dashed line in the inset corresponds to $dA(C_0)/dC_0 = 0$. (b) Estimate of a "covering phase-diagram" in the W_0–C_0 plane showing the parameter range for which a macroscopic film is extracted from the reservoir or is not extracted, respectively. The curve $W_0^{(cov)}$ shows the "covering – non-covering" separatrix described in the main text. The line is a guide for the eye, and the dotted line at $C_0 \leq 0.2$ is a heuristic extrapolation suggesting $W_0^{(cov)}(C_0 \to 0) \simeq 1.4$. The inset shows the dependence of $A(C_0 = 1, W_0)$ on W_0. The line extrapolated to $A(C_0 = 1, W_0) = 0$ is a linear fit of the last four points. In all four plots the symbols are KMC results; dashed and dotted lines connecting the symbols are guides to the eye.

ear extrapolation, as shown in the inset in Fig. 4(b) for the particular value $C_0 = 1$, the interaction strength $W_0^{(cov)}(C_0)$ at which for a given C_0 the prefactor vanishes: $A(C_0, W_0^{(cov)}) = 0$. The data for $W_0^{(cov)}(C_0)$ are shown in Fig. 4(b). Since at a given W_0 the prefactor attains its maximum for $C_0 = 1$, the dependence of $A(C_0 = 1, W_0)$ on W_0 allows one to infer also an estimate of the interaction $\widetilde{W}_0^{(cov)}$ above which no macroscopic film is extracted from the reservoir whatever the density C_0 at the reservoir edge is, i.e., $A(C_0, W_0 > \widetilde{W}_0^{(cov)}) \equiv 0$. This value cannot be measured directly due to the unreasonably long simulation times needed to reach the asymptotic regime in this range of W_0 values, but the linear extrapolation of the available data, as shown in the inset of Fig. 4(b), yields the estimate $\widetilde{W}_0^{(cov)} \simeq 2.3$.

In the range of low densities C_0 at the reservoir edge, the KMC results in Fig. 4 indicate that there is a threshold value $C_0^{(min)} \simeq 0.1$ for the density in the reservoir edge below which, independent of the interaction strength W_0, there is no extraction of a monolayer: all the curves $A(C_0)$ reach zero at a non-zero value of C_0. As we will show below, this is a consequence of the condition **(e)** in the model, i.e., of the requirement that a move from $\boldsymbol{r} \in \Gamma_t$ toward a forward site $\boldsymbol{r'}$ is accepted only if there is at least another particle in the neighborhood $|\boldsymbol{r'} - \boldsymbol{r}| \leq r_c$. As we have mentioned before, this condition is equivalent to requiring a minimum value C_1 for the density on the advancing edge of the film. This density C_1 can be estimated as follows. For a fluid particle at $(x_0, y_0) \in \Gamma_t$ (the filled circle in Fig. 5) to move to the site $(x_0 + 1, y_0)$ (the open circle in Fig. 5), in the shaded area of the disk of radius $r_c = 3$ centered at $(x_0 + 1, y_0)$ there must be at least one more particle in addition to the one attempting the jump. The unshaded sector of the disk is due to the fact that by definition of Γ_t the sites $(x > x_0, y_0)$ are empty. Therefore, at least two of

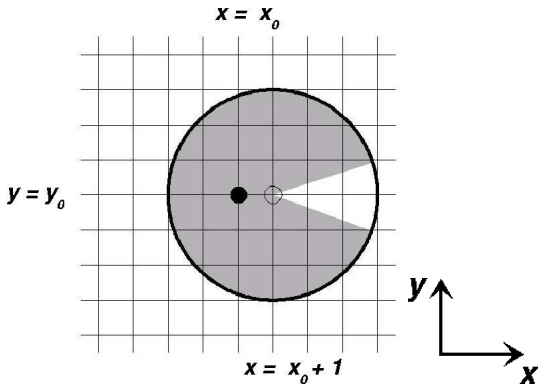

FIG. 5: Schematic drawing of the region around a point (x_0, y_0) (filled circle) belonging to the *advancing* edge Γ_t. The target destination, for the case of an *advancing* Γ_t, is denoted by an empty circle. The shaded area shows the domain in which at least one other site must be occupied so that the particle at (x_0, y_0) can move to $(x_0 + 1, y_0)$ in accordance with our KMC rule **(e)** (see Sect. II). Since $(x_0, y_0) \in \Gamma_t$, all sites $(x > x_0, y_0)$ must be empty so that in the unshaded sector there are no occupied sites.

the $M = 25$ sites in this shaded region are occupied, and thus $C_1 = 0.08$ is an estimate for the minimum density on Γ_t. Since extraction of a film requires a *moving* edge Γ_t, the density at the reservoir edge should be greater than C_1 for spreading to be possible. This explains the threshold value $C_0^{(min)} \simeq 0.1$ observed in the simulations.

B. Asymptotic scaling

We now turn to the analysis of the time dependence of the transversally averaged density profiles $C(x,t)$ of the spreading monolayer. Since the time dependence of the advancing edge follows asymptotically $X(t) \sim \sqrt{t}$ in all the cases in which spreading occurs, it is natural to test if the density profiles $C(x,t)$ actually scale as a function of the scaling variable $\lambda = x/\sqrt{D_0 t}$. In Fig. 6 we show density profiles $C(x,t)$ for (a) $W_0 = 0.6,\ C_0 = 1.0$; (b) $W_0 = 1.4,\ C_0 = 1.0$; (c) $W_0 = 1.0,\ C_0 = 1.0$; and (d) $W_0 = 1.0,\ C_0 = 0.6$ as functions of the scaling variable $\lambda = x/\sqrt{D_0 t}$, and as functions of x in the insets.

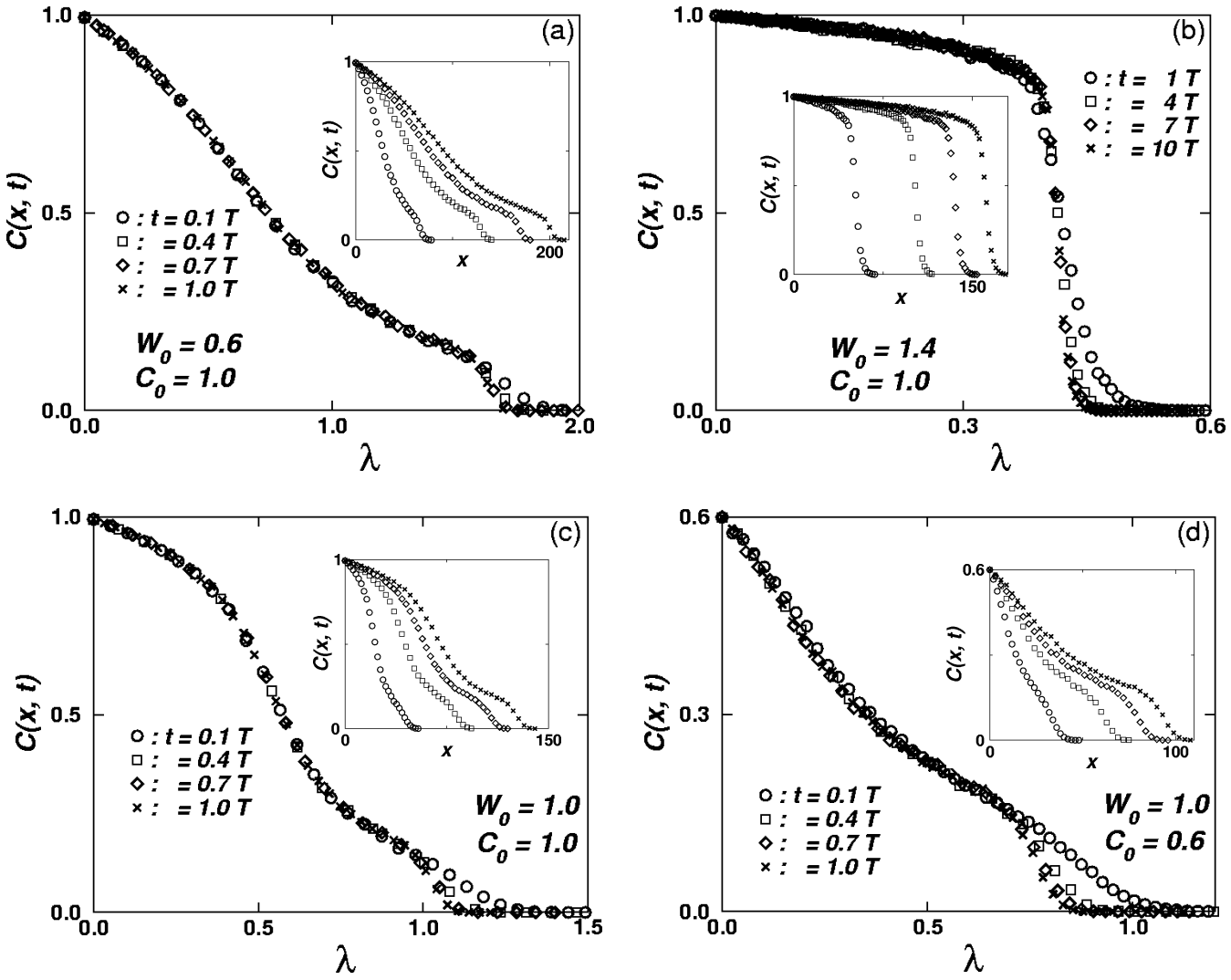

FIG. 6: Density profiles $C(x,t)$ for (a) $W_0 = 0.6,\ C_0 = 1.0$; (b) $W_0 = 1.4,\ C_0 = 1.0$; (c) $W_0 = 1.0,\ C_0 = 1.0$; and (d) $W_0 = 1.0,\ C_0 = 0.6$ as functions of the scaling variable $\lambda = x/\sqrt{D_0 t}$. The insets show these profiles as functions of x. The results correspond to $t = \frac{1}{10}\ T$ (○), $\frac{4}{10}\ T$ (□), $\frac{7}{10}\ T$ (◇), and T (×) in (a), (c), and (d) and to $t = T$ (○), $4\ T$ (□), $7\ T$ (◇), and $10\ T$ (×) in (b), where $T = 2 \times 10^6$. The space and time units are the same as those used in Figs. 2-4.

The results at late times show a very good data collapse and actually only the data corresponding to the earliest time seems to show some significant deviations. This strongly suggests that in the asymptotic limit ($t \gg 1$, $X(t) \gg 1$) the density profiles can be described by a scaling function $\tilde{C}(\lambda = x/\sqrt{D_0 t}; W_0, C_0)$. Here we have explicitly indicated the parametric dependence of the scaling function on the interaction strength W_0 and on the density C_0 at the edge of the reservoir (see Fig. 6). We note that for small C_0 (like $C_0 = 0.6$ in Fig. 6(d)), one

observes deviations from scaling in the range of densities $C(x,t) \lesssim 0.1$. These deviations are most probably due to insufficient statistics, although they may also indicate that the true asymptotic regime has not yet been reached in the simulations. However, since even in this range there is a clear tendency of smaller changes in the shape of the density profile for increasing time t, it is reasonable to expect that the results in Fig. 6 are good approximations for the corresponding scaling function $\tilde{C}(\lambda; W_0, C_0)$.

The scaled density profiles in Fig. 6 reveal three important features. First, we have already noted that the change in shape of the function $A(C_0)$ as W_0 crosses $1.0 < W_0^{(t)} < 1.2$ signals a change in the spreading behavior. As shown by the data in Fig. 6(b), for large W_0 the monolayer has an almost compact structure, and at the advancing edge there is a sharp transition from a large density to a small, almost zero, density. Therefore, in this range of interaction the spreading is accompanied by the emergence of a well defined interface between two phases. In contrast, at small W_0 the density decreases smoothly from the value at the edge of the reservoir to zero and no jump in the density is visible. Thus $W_0^{(t)}$ is a threshold value above which the attractive interaction is strong enough to support the build-up of an interface. In this sense, the change at $W_0^{(t)}$ may be interpreted as the onset of a phase separation.

The second point regards the shape of the density profile as a function of the parameter C_0. For a weak attractive interaction W_0 (Fig. 6(a)) or at small densities C_0 (Fig. 6(d)), the density profiles resemble well the error function solution of a regular diffusion equation for non-interacting particles [1, 2]. As we shall show in the next section, in this range such a description is not only qualitatively but even quantitatively accurate. However, for larger values W_0 (but still below $W_0^{(t)}$) and for large C_0 (see Fig. 6(c)), one finds the formation of a pronounced shoulder in the scaling function in the range of small λ (i.e., $\lambda \lesssim 0.5$), and thus a significant deviation from an error function solution. This shows that in this range of parameters the asymmetry in the jumping probabilities due to the attractive interaction between particles cannot be fully accounted for by an effective boundary force approach as in Ref. [1, 2]. Therefore one has to include explicitly this asymmetry into the description of the dynamics in order to accurately capture the structure of the expanding film. Finally, interaction strengths above $W_0^{(t)}$ have dramatic effects on the spreading behavior, leading to the emergence of interfaces (Fig. 6(b)), and the simple description in terms of non-interacting particles breaks down completely.

The third feature of the profiles to be discussed is the formation of a "foot" at the right end of the profile. The height of the foot is approximately equal to C_1 and this is due to the fact that the density value on an *advancing* edge Γ_t cannot decrease below C_1. The formation of the step implies that the fluctuations of the interface Γ_t around the mean value $X(t)$ are constant or increase in time slower than $\sqrt{t}$, such that the width of the interface divided by $\sqrt{D_0 t}$ vanishes in the long time limit. This sharp interface is occurring naturally due to the fact that the eventually large fluctuations are suppressed by blocking the advancing of isolated particles ahead of the film (see rule **(e)** in Sect. II), and thus the width of the interface would be expected to be of the order of the cut-off $r_c = 3$ of the attractive potential and to be almost constant in time. Although the formation of the "foot" is a somewhat artificial feature introduced in the model by rule **(e)**, the advantage of it is, as discussed in the Introduction, that it leads to the clear formation of an interface with its associated dynamics.

V. CONTINUUM LIMIT

A. Differential equation for the density and scaling behavior

Neglecting all spatial and temporal correlations, i.e., assuming that averages of products of occupation numbers $\eta(\boldsymbol{r};t)$ are equal to the corresponding products of averaged occupation numbers $\rho(\boldsymbol{r};t) = \langle \eta(\boldsymbol{r};t) \rangle$, where $\langle \dots \rangle$ denotes the average with respect to the corresponding probability distribution $\mathcal{P}(\{\eta(\boldsymbol{r};t)\})$ of a configuration $\{\eta(\boldsymbol{r};t)\}$, one can formulate the following mean-field master equation for the local occupational probability (density) $\rho(\boldsymbol{r};t)$:

$$\frac{\Delta\rho(\boldsymbol{r};t)}{\Delta t} = -\rho(\boldsymbol{r};t) \sum_{\boldsymbol{r}', |\boldsymbol{r}'-\boldsymbol{r}|=1} \omega_{\boldsymbol{r}\to\boldsymbol{r}';t}[1-\rho(\boldsymbol{r}';t)] + [1-\rho(\boldsymbol{r};t)] \sum_{\boldsymbol{r}', |\boldsymbol{r}'-\boldsymbol{r}|=1} \omega_{\boldsymbol{r}'\to\boldsymbol{r};t}\rho(\boldsymbol{r}';t) \ , \quad (11)$$

where

$$U(\boldsymbol{r};t) \equiv \langle \tilde{U}(\boldsymbol{r};t) \rangle = -U_0 \sum_{\boldsymbol{r}'', \, 0<|\boldsymbol{r}''-\boldsymbol{r}|\le 3} \frac{\rho(\boldsymbol{r}'';t)}{|\boldsymbol{r}''-\boldsymbol{r}|^6} \quad (12)$$

is replacing $\tilde{U}(\boldsymbol{r};t)$ in the definition for $p(\boldsymbol{r} \to \boldsymbol{r}')$ (Eq. (1)).

As shown in detail in Appendix B, in the continuum space and time limit ($\Delta t \to 0$, $a \to 0$, $\Omega^{-1} \to 0$, $D_0 = \Omega a^2/4$ finite) of Eq. (11), by taking Taylor expansions for $p(\boldsymbol{r} \to \boldsymbol{r}')$ and $\rho(\boldsymbol{r}';t)$ around $\boldsymbol{r}$ and keeping terms up to second-order spatial derivatives of the density $\rho(\boldsymbol{r};t)$ [37, 45, 46], one obtains the following nonlinear and *nonlocal* equation for $\rho(\boldsymbol{r};t)$,

$$\partial_t \rho = D_0 \nabla \left[\nabla\rho + \beta\rho\,(1-\rho)\nabla U \right] + \mathcal{O}(a^2) \quad (13)$$

Since the derivation of Eq. (13) presented in Appendix B is not a rigorous proof (as we shall discuss below, such a proof appears to be extremely difficult to obtain) but rather a heuristic derivation in the spirit of Ref. [46], several comments are in order before proceeding. The

only lattice gas system with long-ranged interactions for which it has been rigorously shown that Eq. (13) represents the correct continuum limit at all temperatures is the hard-core lattice gas model with a Hamiltonian composed of short-ranged (on-site) repulsion and long-(infinite) ranged Kac potentials evolving via rates which satisfy detailed balance [47, 48, 49]. Recently, it has been argued that similar equations will also hold for systems with relatively short-ranged interactions [50, 51, 52]. The system discussed in Refs. [50, 51, 52] is a hard-core lattice gas model with attractive inter-particle interaction in the form of either a finite range constant potential or of Morse potentials, a microscopic dynamics defined by nearest neighbor jumping rates depending on the energy at the departure site (Arrhenius dynamics) or on the difference in energy between the two sites (Metropolis dynamics), and a fixed density gradient imposed by fixed densities at the boundaries of the simulation box. As shown in Ref. [52], the solutions of such continuum equations compare fairly well with results of corresponding kinetic Monte Carlo simulations in cases where the interaction range is greater than several lattice units. Typical values are 5-10 lattice units, depending on the dimensionality of the problem, the type of potential, and the type of dynamics defined by the microscopic rates. Moreover, it has been shown by Leung [46] that heuristic derivations, based on formal Taylor expansions, of continuum equations from microscopic dynamics give very good results both for the dynamics of Ising models with nearest neighbor interactions and Kawasaki rates and for that of driven lattice gases. Based on these results we assume that Eq. (13) is at least a good approximation for the the continuum limit of our system, although it was not rigorously derived and although the range of the attractive potential in our problem is rather short ($r_c = 3$). Finally, since the continuum limit for our system seems to be described by the same equation as that for the dynamics in systems evolving via rates preserving the detailed balance condition, one may conclude that indeed the deviations (calculated in Appendix B) from detailed balance in the rates defined by Eq. (4) are small and do not carry over to the macroscopic scale.

The constraint of a fixed density C_0 at the edge $x = 0$ of the reservoir implies the boundary condition

$$\rho(x = 0, y; t) = C_0 \,. \tag{14}$$

As we have pointed out in Subsec. IV.A, the condition **(e)** in the model leads to a well defined interface and implies that for a spreading film the minimum density on the advancing edge is $C_1 \gtrsim 0.08$. In the absence of other additional constraints imposed by the formation of interfaces, i.e., for interactions $W_0 < W_0^{(t)}$, and for large times, these considerations and the KMC results (see also Figs. 6(a), (c), and (d)) strongly suggest that the density on the advancing edge $X(t)$ can be considered as fixed and equal to C_1, leading to the boundary condition

$$\rho(x = X(t), y; t) = C_1 \,. \tag{15}$$

In what follows, we shall use the value $C_1 = 0.11$ obtained in the KMC simulations. We note in passing that the boundary condition Eq. (15) also naturally occurred in the "effective boundary force" model of Burlatsky *et al.* [1, 2], the expression of C_1 in this case being $C_1 = 1 - \mu$, with μ the ratio between the forward and the backward jumping rate for particles on the advancing edge.

Since there are no boundaries along the $y-$direction and the boundary condition at the reservoir (Eq. (14)) is independent of y, an important consequence of the $y-$independence of Eq. (15) is that the solution $\rho(\boldsymbol{r}; t)$ does not actually depend on y, which implies that the monolayer is homogeneous along the $y-$direction, in agreement with the KMC results. Therefore one has to solve an effectively one-dimensional problem. The study of the occurrence of spontaneous transversal instabilities of the advancing edge would require to replace Eq. (15) by a moving, transversally varying boundary condition. This might become relevant if the monolayer is driven by external forces or encounters an obstacle. However, in view of the KMC results we have no reason to consider such effects for the present system.

Although the reduced dimensionality is a significant simplification, Eq. (13) remains quite complex because it is nonlocal due to the term involving the interaction potential $U(\boldsymbol{r}; t)$. However, assuming that the density $\rho(\boldsymbol{r}; t)$ is a slowly varying function of the spatial coordinates (which certainly is a reasonable hypothesis everywhere except near interfaces, see Figs. 2 and 6), the potential $U(\boldsymbol{r}; t)$ may be expanded as

$$\begin{aligned} U(\boldsymbol{r}; t) &= -U_0 \sum_{\boldsymbol{r'}, 0<|\boldsymbol{r'}-\boldsymbol{r}|\leq 3} \frac{\rho(\boldsymbol{r'}; t)}{|\boldsymbol{r'} - \boldsymbol{r}|^6} \\ &\simeq -U_0 \rho(\boldsymbol{r}; t) \sum_{\boldsymbol{r'}, 0<|\boldsymbol{r'}-\boldsymbol{r}|\leq 3} \frac{1}{|\boldsymbol{r'} - \boldsymbol{r}|^6} + \mathcal{O}(a^2) \,. \end{aligned} \tag{16}$$

As discussed in Appendix B, the rotational symmetry of the lattice and of the factor $|\boldsymbol{r'} - \boldsymbol{r}|^{-6}$ implies that the summation over $\boldsymbol{r'}$ will cancel the contributions of the first-order derivatives, and thus the leading gradient term does not appear in the expansion above. Because in the derivation of Eq. (13) only terms up to second-order spatial derivatives of the density have been kept, i.e., second-order in the lattice constant a, and a factor a^2 has been already absorbed into the diffusion coefficient D_0, only the zeroth-order term in the expansion above will contribute. This leads to the *local* equation

$$\partial_t \rho = D_0 \nabla \{ [1 - g\, W_0 \rho (1 - \rho)] \, \nabla \rho \} + \mathcal{O}(a^2), \tag{17}$$

where $g = \sum_{1 \leq |\boldsymbol{r}| \leq r_c} |\boldsymbol{r}|^{-6}$ is a geometrical factor dependent on the lattice type (e.g., square, triangular, etc.)

and on the cut-off range of the potential. For the present case of a square lattice and a cut-off at $r_c = 3$ one has $g \simeq 4.64$.

Rescaling the time as $t \to \tau = D_0 t$ and defining an effective diffusion coefficient

$$D_e(\rho) = 1 - g\, W_0 \rho(1-\rho), \tag{18}$$

Eq. (17) may be written in the usual form of a diffusion equation

$$\partial_\tau \rho = \nabla \left[D_e(\rho) \nabla \rho \right] + \mathcal{O}(a^2)\,. \tag{19}$$

The functional form of $D_e(\rho)$ (Eq. (18)) implies that for $W_0 > 4/g$ there will be values ρ_i of the density for which $D_e(\rho_i) < 0$ (see Fig. 7). For parameters such that

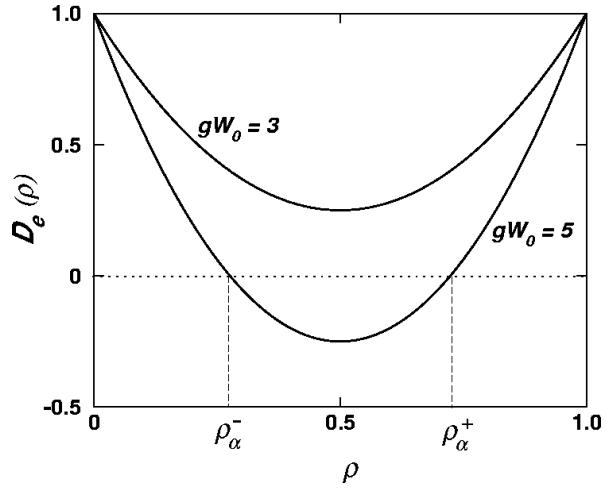

FIG. 7: Effective diffusion coefficient $D_e(\rho)$ (Eq. (18)) for $gW_0 = 3$ (upper curve) and $gW_0 = 5$ (lower curve), i.e., below and above the threshold value $gW_0^{(t)} = 4$, respectively. The values ρ_α^- and ρ_α^+ indicate the range of densities ρ_i for which $D_e(\rho_i) < 0$, corresponding to instabilities in Eq. (19).

$W_0 < 4/g$, Eq. (19) is a proper diffusion equation, while for $W_0 > 4/g$ instabilities are expected in the range of densities where $D_e(\rho_i) < 0$, i.e., for $\rho_i \in (\rho_\alpha^-\ ,\ \rho_\alpha^+)$ where

$$\rho_\alpha^\pm = \frac{1}{2}\left(1 \pm \sqrt{1 - \frac{4}{gW_0}}\ \right)\,. \tag{20}$$

It is known [47, 53] that these instabilities are discontinuities in the density profile ("shocks"), i.e., they correspond to the formation of interfaces, which is exactly what is observed in the KMC results. Thus the value for the threshold interaction strength $W_0^{(t)}$ (introduced in Sec. IV) for which interfaces emerge is predicted by the continuum theory as $W_0^{(t)} = 4/g \simeq 0.86$. This value is significantly smaller than the lower bound estimate $1.0 < W_0^{(t)}$ from KMC simulations, which is not unexpected because of the mean-field character of the derivation of the continuum equation. However, a simple, intuitive argument allows an effective inclusion of correlations into the mean-field description and leads to a simple correction to the mean-field value $g = 4.64$. The dynamics is possible only by jumps into empty locations. This means that the summation in g should include at most three contributions from nearest neighbor sites, giving $g \simeq 3.64$ and an estimate for the threshold interaction $W_0^{(t)} \simeq 1.1$, in good agreement with the KMC results. Thus for the rest of the analysis we will use this corrected value of g.

We now proceed with the analysis of the density profiles for the asymptotic scaling limit. Since the solution $\rho(\boldsymbol{r}; t)$ depends only on x, Eq. (19) yields an equation for the transversally averaged density $C(x, \tau)$:

$$\partial_\tau C(x;\tau) = \partial_x \left[D_e(C) \partial_x C(x;\tau) \right] + \mathcal{O}(a^2). \tag{21}$$

Introducing the scaling variable $\lambda = x/\sqrt{\tau}$ leads to the following equation for the scaling solution $\tilde{C}(\lambda)$ in the asymptotic limit $t \gg 1$:

$$\frac{\lambda}{2}\frac{d\tilde{C}}{d\lambda} + \frac{d}{d\lambda}\left[D_e(\tilde{C}) \frac{d\tilde{C}}{d\lambda} \right] + \mathcal{O}[(a/\sqrt{\tau})^2] = 0 \tag{22}$$

with the boundary conditions

$$\tilde{C}(0) \ = \ C_0\,, \tag{23a}$$

$$\tilde{C}(A) \ = \ C_1\,. \tag{23b}$$

Since the solution of Eq. (22) depends on whether $W_0 < W_0^{(t)}$ or $W_0 > W_0^{(t)}$, we shall discuss these two cases separately.

B. Scaling solution for $W_0 < W_0^{(t)}$

For $W_0 < W_0^{(t)}$, in Eq. (22) the term $\mathcal{O}[(a/\sqrt{\tau})^2]$ may be neglected and Eq. (22) together with the boundary conditions given in Eq. (23) is a well posed problem and thus admits a regular solution $\tilde{C}(\lambda; W_0, C_0)$. Although the solution cannot be found in closed form, the numerical integration of Eq. (22) is straightforward. Results for small and intermediate values of the attractive coupling W_0 and for several values of C_0 are presented in Fig. 8. For comparison, we also show results coresponding to the mean-field "effective boundary force" (EBF) approach [1] subject to the same boundary conditions (Eq. (23)), for which the density profile is given by [54]

$$\tilde{C}_{mf}(\lambda) = C_0 - (C_0 - C_1)\frac{\mathrm{erf}(\lambda/\sqrt{2})}{\mathrm{erf}(A/\sqrt{2})}, \tag{24}$$

where $\mathrm{erf}(z) = \frac{2}{\sqrt{\pi}} \int_0^z dy\, e^{-y^2}$ is the error function.

There is excellent agreement in all cases between the theoretical results from Eq. (22) and the KMC results. Similar conclusions hold for all values of C_0 and $W_0 \leq 1.0$. (These results are not shown.) These findings offer additional strong support both to the assumption that

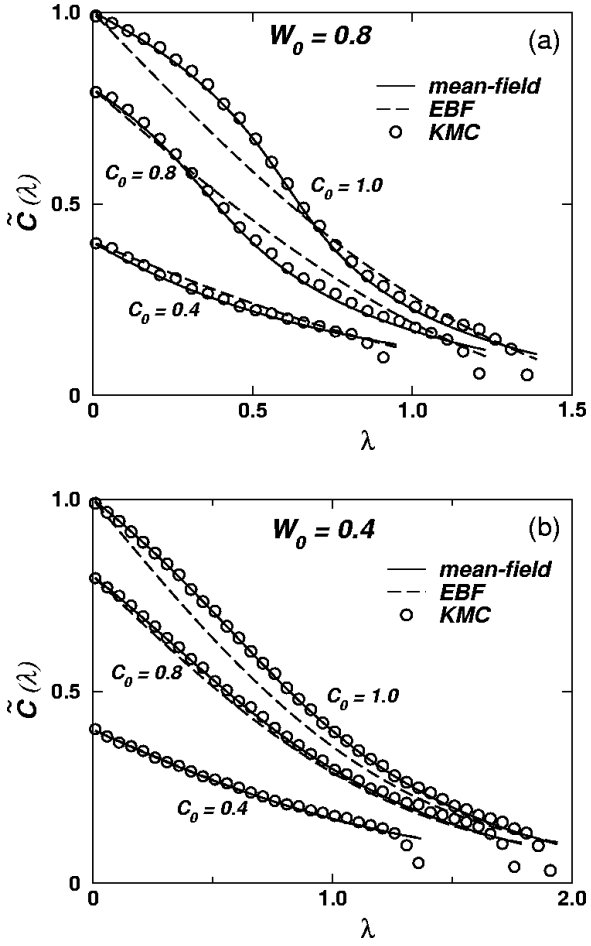

FIG. 8: Asymptotic scaling solution $\tilde{C}(\lambda)$ for (a) $W_0 = 0.6$, $\tilde{C}(\lambda = 0) = C_0 = 1.0, 0.8, 0.4$ and (b) $W_0 = 1.0$, $\tilde{C}(\lambda = 0) = C_0 = 1.0, 0.8, 0.4$ with $\lambda = x/\sqrt{D_0 t}$. Shown are theoretical mean-field results from Eq. (22) (solid lines), results of the "effective boundary force" (EBF) theory from Eq. (24) (dashed lines), and corresponding KMC results at time $T = 2 \times 10^6$ ($\bigcirc$) (assumed to be close to the asymptotic limit).

Eq. (22) is an accurate description of the continuum limit for $W_0 < W_0^{(t)}$ and to our heuristic correction $g \simeq 3.64$ for taking correlations into account (see the paragraph preceding Eq. (21)). When compared to the EBF results from Eq. (24), we see that, as expected, at low densities of the reservoir (see, e.g., the curves in Fig. 8 corresponding to $C_0 = 0.4$) the predictions of Eq. (22) and the EBF results are almost identical because the monolayer is dilute and thus the particle-particle interactions are less effective. For similar reasons, at low values for the strength of the inter-particle attraction or at high temperature, i.e., when W_0 is small, the EBF description performs well even for high densities (see in Fig. 8(b) the curve corresponding to $C_0 = 0.8$). However, at very high densities of the reservoir or for large values of the attractive coupling W_0, there are significant discrepancies even in the *qualitative* behavior between the EBF predictions and the simulations results. In particular, the formation of a "shoulder" in the case in which W_0 is large (see in Fig. 8(a) the curves corresponding to $C_0 = 1$ and $C_0 = 0.8$) is remarkably well reproduced by the theoretical curve obtained from Eq. (22), but it is completely missed by the EBF solution (Eq. (24)). Therefore we conclude that even in this case, i.e., below the threshold value $W_0^{(t)}$ for interface formation, the inter-particle attraction has to be explicitly included into the model in order to obtain a correct prediction for the mass distribution inside the monolayer which is extracted.

The above results should also be discussed in the context of the similar work in Refs. [51] and [52] mentioned in the beginning of this subsection. We have emphasized that the derivation of the continuum limit is mean-field-like in character, and that *only* after correcting for correlations, i.e., after adopting the improved value $g \simeq 3.64$, the continuum limit accurately predicts both the threshold value $W_0^{(t)}$ for the interaction coupling and the scaled asymptotic density profiles $\tilde{C}(\lambda; W_0, C_0)$. Such a correction has not been included in the similar continuum equations discussed in Refs. [51] and [52], and we suggest that this explains the discrepancies observed by the authors in the case in which the range of the inter-particle potential is short (see, e.g., the density profiles corresponding to cut-off ranges $r_c = 2$ and $r_c = 5$ in Fig. 4(a) in Ref. [52]). For the longer-ranged potentials ($r_c \geq 5$) used in Refs. [51] and [52], further than nearest neighbors contribute significantly to g, and thus the exclusion of a nearest-neighbor term becomes relatively less important, which explains the good agreement obtained in the cases $r_c \geq 5$ without any correction included.

Before proceeding to the case $W_0 > W_0^{(t)}$, we would also like to briefly comment on the connection between our above results, the experimental results for the precursing films of Pb on Cu(111) reported in Ref. [55], and the MD results for precursing films of Ag on Ni(100) presented in Ref. [56]. The density profiles measured experimentally (see Fig. 3(b) in Ref. [55]) and in the MD simulations (see Fig. 3 in Ref. [56]) for the 2D spreading of Pb or Ag films show a striking resemblance with the ones we have obtained in the KMC simulations. Moreover, by assuming a macroscopic diffusive dynamics described by an equation of the same form as the one derived in Eq. (21), effective diffusion coefficients $D_e(C)$ have been obtained from the density profiles, and the data shown in Fig. 3(a) in Ref. [55] are in qualitative agreement with a quadratic dependence for $D_e(C)$ as in Eq. (18). Therefore, the very simple microscopic model we discussed seems to capture the essential features of the dynamics in these cases. Moreover, this suggest that this form of $D_e(C)$ for Pb on Cu(111) is not necessarily due to surface alloying – a mechanism which is not included into the dynamics of our model – but is rather already a consequence of the interplay between the concentration gradients and the inter-particle interaction, which leads to "jamming" and thus significantly slows down the dif-

fusion for large values of the density $C(x,t)$.

C. Scaling solution for $W_0 > W_0^{(t)}$

We now turn to the discussion of Eq. (22) for the case $W_0 > W_0^{(t)}$. Because in this case the effective diffusion coefficient $D_e(\tilde{C})$ becomes negative within a range of densities, the problem is known to be mathematically ill-posed and to lead to discontinuities ("shocks") in the long-time limit if the small terms $\mathcal{O}[(a/\sqrt{t})^2]$ (see Eq. (22)) are set to zero [53]. For this problem the existence and uniqueness of a "weak" solution $\tilde{C}(\lambda)$ ("weak" in the sense that $\tilde{C}(\lambda)$ has a discontinuity at a point $\lambda = \lambda_s$ but satisfies Eq. (22) for $\lambda \neq \lambda_s$) have been recently addressed by Witelski [57, 58] using singular perturbation methods. We will use here directly the explicit construction of the shock solution derived in Ref. [57] for the case in which the term $\mathcal{O}(a^2/\sqrt{t})$ is proportional to $\partial_x^4 C(x,t)$, the details of the calculation being presented in Appendix C.

Defining

$$\mu(C) = \int_0^C dC'\, D_e(C') \tag{25}$$

Eq. (21) may be rewritten as

$$\partial_\tau C = \partial_x^2 \mu(C) + \mathcal{O}(a^2)\,, \tag{26}$$

i.e., it has the form of a diffusion equation for $C(x,\tau)$ with a mobility $M = 1$ and a "chemical potential" $\mu(C)$. Moreover, as we will discuss below, the values of $\mu(C)$ across the discontinuity satisfy conditions which are similar to those determining the equilibrium liquid-vapor coexistence line in the van der Waals-Maxwell mean-field theory of liquid-vapor transitions. Because of these similarities, in what follows we shall informally denote $\mu(C)$ as chemical potential.

Following Refs. [57, 58], we look for a weak solution of Eq. (22), subject to the boundary conditions given in Eq. (23), in the form of a "shock" defined as

$$\tilde{C}(\lambda) = \begin{cases} C_\ell(\lambda), & \lambda < \lambda_s, \\ C_r(\lambda), & \lambda > \lambda_s, \end{cases} \tag{27}$$

where $C_\ell(\lambda)$ and $C_r(\lambda)$ satisfy Eq. (22) in the intervals $[0, \lambda_s)$ and $(\lambda_s, A = X(t)/\sqrt{t}]$, respectively, subject to the boundary conditions

$$\begin{aligned} C_\ell(0) &= C_0,\ C_\ell(\lambda_s) = C_M, \\ C_r(\lambda_s) &= C_m < C_M,\ C_r(A) = C_1, \end{aligned} \tag{28}$$

respectively. As discussed in Appendix C, the singular perturbation analysis of Eq. (22) implies that the values C_M and C_m of the density at the left and the right of the shock, respectively, are determined from the following conditions expressed in terms of $\mu(C)$:

$$\mu(C_M) = \mu(C_m), \tag{29a}$$

$$\int_{C_m}^{C_M} dC'\,[\mu(C') - \mu(C_M)] = 0, \tag{29b}$$

i.e., continuity of the "chemical potential" $\mu(C)$ across the shock and a Maxwell equal area-rule across the shock, as mentioned at the beginning of this subsection. Solving Eq. (29), we find that the only solution satisfying the condition $C_M > C_m$ is

$$C_M = \frac{1}{2} + \frac{\sqrt{3}}{2}\sqrt{1 - \frac{4}{gW_0}}\,, \tag{30a}$$

$$C_m = \frac{1}{2} - \frac{\sqrt{3}}{2}\sqrt{1 - \frac{4}{gW_0}}\,. \tag{30b}$$

Comparison with the similar expressions for $C_\alpha^\pm$, where $D_e(C_\alpha^\pm) = 0$ (Eq. (20)), shows that for all $W_0 > W_0^{(t)}$ one has $C_m < C_\alpha^- < C_\alpha^+ < C_M$, thus the shock occurs both above and below the interval corresponding to unstable states. For the states corresponding to densities $C \in \mathfrak{C} = (C_m\,, C_\alpha^-) \cup (C_\alpha^+\,, C_M)$ the effective diffusion coefficient is positive, but the density gradients are very large in the long-time limit and the state becomes part of the shock; thus densities $C \in \mathfrak{C}$ correspond to metastable states.

The last unknown, the position λ_s of the shock, is obtained from the conservation of mass. In an infinitesimal time interval $\delta\tau$, the displacement $\delta s = x_s(\tau+\delta\tau) - x_s(\tau)$ of the position $x_s = \lambda_s\sqrt{\tau}$ of the shock leads to an increase $(C_M - C_m)\delta s$ in the mass inside the stripe $x_s(\tau+\delta\tau) - x_s(\tau)$. This should be equal to the net mass transfer $\delta\tau[j(x_s) - j(x_s + \delta s)]$, where the mass current $j(x) = -\partial_x \mu(C)$ (see Eq. (26)) is discontinuous at x_s. Since $\delta s/\delta\tau = (1/2)\lambda_s \tau^{-1/2}$ and $\partial_x C = \tau^{-1/2}\frac{dC}{d\lambda}$, one obtains the following expression for the position λ_s of the shock

$$\lambda_s = -\,2\,\frac{D_e(C_M)\,\dfrac{dC}{d\lambda}\Big|_{C_M} \;-\; D_e(C_m)\,\dfrac{dC}{d\lambda}\Big|_{C_m}}{C_M - C_m}. \tag{31}$$

We note that the above result can be also obtained via a direct integration of Eq. (22) across the shock, i.e., from $\lambda = \lambda_s - \xi$ to $\lambda = \lambda_s + \xi$ in the limit $\xi \to 0$, using for the density profile there the approximation by a step function $C(\lambda) = C_M - (C_M - C_m)H(\lambda - \lambda_s)$, where $H(x)$ is the Heaviside function $(H(x<0) = 0\,, H(x \geq 0) = 1)$. It is important to note here that for sufficiently large values W_0 of the attractive interaction the density C_m may become smaller than C_1. Since the density at the advancing edge cannot be smaller than C_1, in this case the branch $C_r(\lambda)$ disappears and the shock position is obtained by setting $C_m = 0$ in Eq. (31).

Once C_m and C_M are known, Eqs. (22), (28), and (31) can be, in principle, solved for the corresponding quantities $C_\ell(\lambda)$, $C_r(\lambda)$, and the position λ_s of the shock. Since

Eq. (22) cannot be solved in closed form, the above system of equations has to be solved numerically. Such a numerical solution is shown in Fig. 9 for the cases (a) $W_0 = 1.2$, $C_0 = 1.0$, for which $C_m \simeq 0.25 > C_1$, and (b) $W_0 = 1.4$ and $C_0 = 1.0$, for which $C_m \simeq 0.098 \lesssim C_1$. It can be seen that the agreement between the theoretical asymptotic "shock" solution and the KMC measured density profiles is good for the large value $W_0 = 1.4$, but it is not so good in the case $W_0 = 1.2$. This is very likely due to the fact that in the latter case the simulation has not yet reached the true asymptotic regime, while for $W_0 = 1.4$ the approach to the asymptotic shape is faster because the low density branch C_r is suppressed. In both cases the KMC results confirm the value C_M as the onset of large density gradients, and there is good agreement between the theoretical prediction and the simulations in the range of densities $C > C_M$. This also supports the above conclusion that the discrepancies in the range $C < C_M$ are due to simulations times which are not large enough.

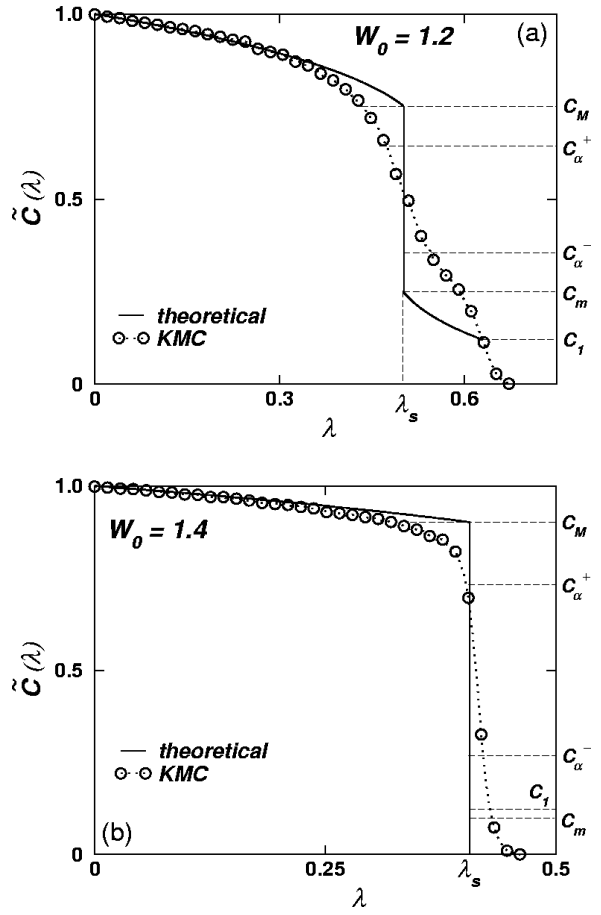

FIG. 9: Asymptotic scaling solution $\tilde{C}(\lambda)$ for (a) $W_0 = 1.2$, $C_0 = 1.0$, and (b) $W_0 = 1.4$, $C_0 = 1.0$. Shown are theoretical results obtained from Eqs. (22), (28), and (31) (solid lines), and corresponding KMC results at time $T = 2 \times 10^7$ (○) (assumed to be close to the asymptotic limit). The dotted line is a guide to the eye. The dashed lines indicate the corresponding values C_m and C_M from Eq. (30), $C_\alpha^\pm$ from Eq. (20) where $D_e(C_\alpha^\pm) = 0$, which determines the onset of the density range leading to instabilities (see Fig. 7), C_1 from the boundary condition Eq. (23b), and the position λ_s of the discontinuity given by Eq. (31).

The jump $C_M - C_m$ in the density at λ_s explains the formation of the plateau (for $W_0 > W_0^{(t)}$) in the dependence of $A(C_0, W_0)$ on C_0: if the density C_0 at the reservoir is within the range $C_m \le C_0 < C_M$, in the immediate vicinity of the reservoir edge the density drops to C_m and in the long-time limit the extraction of the film proceeds effectively as if the reservoir density would have been C_m. Also, since $1/2 - C_m = -1/2 + C_M$, it follows that the plateau should be symmetric with respect to $C_0 = 0.5$; indeed the KMC data in Fig. 4(a) exhibit this symmetry (as long as W_0 is such that $C_m > 0.1$). Moreover, since the density must satisfy $C \le 1$, one may conclude that for interaction values W_0 such that $C_M > 1$ the extraction of a monolayer is no longer possible. This implies that the exact value for the upper limit of the interaction $\widetilde{W}_0^{(cov)}$ above which no macroscopic film is extracted from the reservoir is given by $\widetilde{W}_0^{(cov)} = 6/g \simeq 1.65$. This value is significantly below the value $\widetilde{W}_0^{(cov)} = W_0^{(cov)}(C_0 = 1) \simeq 2.3$ extracted from the linear extrapolation of the KMC data (see Fig. 4(b)), the discrepancy very likely reflecting that the KMC simulations have not yet reached the true asymptotic limit (or that a linear extrapolation is not appropriate). Thus it is to be expected that in the range $C_0 \gtrsim 0.85$ the separatrix $W_0^{(cov)}$ shown in Fig. 4(b) significantly overestimates the correct curve.

VI. SUMMARY AND CONCLUSIONS

Using kinetic Monte Carlo (KMC) simulations and a non-linear diffusion equation within the continuum limit, we have studied a lattice-gas model with interacting particles for the two-dimensional spreading on homogeneous substrates of a fluid monolayer which is extracted from a reservoir (Fig. 1). We have obtained the following main results:

1. The two-dimensional KMC simulations confirm the time dependence $X(t \to \infty) = A\sqrt{t}$ of the spreading, where $X(t)$ is the average position of the advancing edge of the monolayer at time t, and reveal a non-trivial dependence of the prefactor A on the strength U_0 of interparticle attraction and on the fluid density C_0 at the reservoir (see Figs. 2, 3, and 4). A careful analysis of this behavior has allowed us to identify, in terms of $W_0 = U_0/k_BT$, a transition point $W_0^{(t)} \simeq 1.1$ associated with the occurrence of interfaces inside the extracted monolayer, and to estimate a "covering phase-diagram" in the W_0–C_0 plane (Fig. 4) together with a "covering – non-covering" separatrix $W_0^{(cov)}$ below which a macroscopic film is extracted from the reservoir, while above $W_0^{(cov)}$ it is not extracted.

2. The asymptotic (i.e., at long time and large spatial scales) transversally averaged density profiles $C(x,t)$ measured in the KMC simulations exhibit a scaling behavior as function of the scaling variable $\lambda = x/\sqrt{D_0 t}$, where D_0 is the one-particle diffusion coefficient on the bare substrate (Fig. 6). They clearly show that for this model the density in the extracted monolayer is not spatially constant, in contrast to the predictions of other theoretical models mentioned in the Introduction. This provides an unambiguous – and otherwise difficult – way to experimentally discriminate between the various theoretical models proposed. Moreover, the simulations show that the present model predicts qualitatively different structures for the experimentally accessible density profiles above and below the threshold value $W_0^{(t)}$ (see Figs. 7 and 8), in particular the formation of sharp interfaces inside the extracted monolayer for $W_0 > W_0^{(t)}$.

3. The asymptotic, scaled density profiles $\tilde{C}(\lambda)$ have been analyzed within a continuum limit with the corresponding non-linear diffusion equation derived from the microscopic master equation. Within this approach we have included the effect of correlations in an effective manner into the standard mean-field description by adapting the value of the integrated attractive interaction to account for the presence of empty nearest-neighbor sites (see Fig. 5). This leads to an excellent agreement between the theoretical predictions based on the continuum limit and the KMC results both for the value $W_0^{(t)}$ and for the scaled density profiles (Fig. 8). Additionally we have shown that, even below the threshold value $W_0^{(t)}$ for interface formation, the inter-particle attraction has to be explicitly included into the model in order to obtain correct predictions for the mass distribution inside the extracted monolayer. The formation of the interfaces in the range $W_0 > W_0^{(t)}$ has been related to instabilities of the diffusion equation associated with densities for which the corresponding effective diffusion coefficient becomes negative (Fig. 7). We have constructed the corresponding discontinuous density profiles ("shocks") and critically compared them with the KMC measured ones (Fig. 9). Based on the results of a singular perturbation analysis, we have obtained a good estimate $\widetilde{W}_0^{(cov)} \simeq 1.65$ for the upper limit of the interaction above which no macroscopic film is extracted from the reservoir.

Finally, we comment on the connection between this model and experimental systems. As briefly discussed in Subsect.V.B, the present model appears to provide a successful description for the diffusion of solid metals on metal surfaces as studied in Refs. [55] and [56]. We have found a *qualitative* agreement between the experimental results in the case of diffusion of Pb on Cu(111) [55] and our theoretically derived density profiles and effective diffusion coefficient. It seems to be promising to explore *quantitatively* the applicability of the present model for such metal on metal systems. To this end the experimental setup described in Refs. [55] and [56] would have to be modified in order to have straight instead of circular spreading geometries and a deposit-substrate combination chosen such as to avoid surface alloying effects.

As noted in the Introduction the experiments with fluids performed so far deal with polymer oils. As long as the entanglement of the polymer chains is not important, one may consider a coarse-grained description in which the chain is replaced by an effective particle of the size of the corresponding radius of gyration and only the motion of the center of mass is considered. Although the motion of these effective particles might not resemble simple, activated jumping processes so that the microscopic model description is not directly applicable, it is reasonable to expect that the macroscopic evolution will be diffusive. Therefore, one may expect that the continuum limit of the present model can be used to describe the spreading behavior observed in experiments with polymer oils, but the macroscopic parameters entering into the diffusion equation should be regarded as fit parameters and not quantities calculated from microscopic dynamics as considered here.

In order to obtain a direct, quantitative test of the present theoretical predictions for precursor liquid films, new experiments would have to be performed using simple liquids chosen such that they have a spreading rate large compared with the evaporation rate. This should be combined with observation techniques chosen such that the density profiles, and not only the spreading rate, could be measured, which would require an in plane (lateral) resolution in the order of few nm for the case of simple liquids, i.e., several lattice constants, and in the order of 10-50 nm for the case of polymer oils, i.e., several inter-"effective" particles distances, because the density variations are expected to occur on larger length scales. One technique which possibly may fulfill these requirements is reflection interference contrast microscopy [59], assuming that the microscope objective may scan the area of interest (of the order of mm^2) in times sufficiently small compared to those on which the density profile changes. The technique has been used before in studies of (equilibrium) wetting properties on micropatterned solid surfaces [59], and already at the time of its first implementation a lateral resolution of at least 200 nm (see Fig. 13(b) in Ref. [59]) combined with a normal resolution of the order of 1 nm has been achieved.

Acknowledgments

This work has been supported by the Deutsche Forschungsgemeinschaft within the priority program "Wetting and Structure Formation at Interfaces", Grant DI 315/7-3.

APPENDIX A: KINETIC MONTE CARLO METHOD

In this section we discuss in some detail the variable-step continuous-time kinetic Monte Carlo algorithm [41, 42, 43] that we have used. The main idea is to consider the sequence of independent, uncorrelated events represented by jumps of particles away from the wells in which they were residing. Each of these events has an identical time- and environment-independent rate Ω as shown by Eq. (5), in contrast to the location-dependent rates of particular transitions $\boldsymbol{r} \to \boldsymbol{r'}$ (Eq. (4)).

Consider the system at time t when there are N particles in the film ($x > 0$) and an event just occurred. Since the attempts of any particle to leave its well are uncorrelated to similar events of other particles, and since for each particle the rate for a successful jump is Ω, for each one of the particles the probability that until time $t' > t$ no successful attempt occurs is $P_1(\tau) = \exp(-\Omega\tau)$, where $\tau = t' - t$. Therefore, since the jumps are uncorrelated, the probability that *none* of the N particles experienced a successful attempt in τ is $P_N(\tau) = [P_1(\tau)]^N = \exp(-N\Omega\tau)$ and the probability that the first successful jump will take place at t' will be given by

$$P = N\Omega P_N(\tau) = N\Omega \exp(-N\Omega\tau). \tag{A1}$$

Thus the time interval τ between successful jumping attempts (between "events") is a random variable distributed according to Eq. (A1). Since all the N particles have identical rates Ω for events, the probability for a certain particle to be the one undergoing the jump is $\Omega/(N\Omega) = 1/N$, i.e., the particle to jump is selected at random. Let us assume the selected particle is at location $\boldsymbol{r}$. There are $z = 4$ nearest-neighbor locations, and thus $z = 4$ possible realizations of the jump; the one to be actually attempted is selected according to the probability defined by Eq. (1). Specifically, calling the four probabilities $p_1, \ldots, p_4$, with p_1 corresponding to the jump $(x, y) \to (x + 1, y)$ and the others being indexed counter clockwise, one compares the successive sums $s_0 \equiv 0$, $s_j = \sum_{k=1}^{k=j} p_k$, $j = 1, 2, 3, 4$, with a random number $v \in [0, 1]$ and selects p_k for which $s_{k-1} < v \leq s_k$. As described in the text, the jump takes place if the selected destination site is empty, and is rejected if the destination site is occupied.

We note here that, as shown in Ref. [43], incrementing the time between events using intervals generated according to Eq. (A1) and not a constant time interval equal to the average time $1/(N\Omega)$ between events, like in a classical Monte Carlo simulation, is essential in assuring that the simulated time is the correct real time, and thus that the simulations capture the correct time development of spreading.

APPENDIX B: HEURISTIC DERIVATION OF THE CONTINUUM LIMIT

The (mean-field) master equation for the local occupational probability (density) $\rho(\boldsymbol{r}; t)$ is given by

$$\begin{aligned}\frac{\partial \rho(\boldsymbol{r};t)}{\partial t} = &-\rho(\boldsymbol{r};t) \sum_{\boldsymbol{r'},|\boldsymbol{r'}-\boldsymbol{r}|=1} \omega_{\boldsymbol{r}\to\boldsymbol{r'};t}[1-\rho(\boldsymbol{r'};t)] \\ &+[1-\rho(\boldsymbol{r};t)] \sum_{\boldsymbol{r'},|\boldsymbol{r'}-\boldsymbol{r}|=1} \omega_{\boldsymbol{r'}\to\boldsymbol{r};t}\rho(\boldsymbol{r'};t),\end{aligned} \tag{B1}$$

where

$$\omega_{\boldsymbol{r}\to\boldsymbol{r'};t} = \Omega \frac{\exp\left\{\frac{\beta}{2}\left[U(\boldsymbol{r};t) - U(\boldsymbol{r'};t)\right]\right\}}{\sum_{\boldsymbol{r'},|\boldsymbol{r'}-\boldsymbol{r}|=1} \exp\left\{\frac{\beta}{2}\left[U(\boldsymbol{r};t) - U(\boldsymbol{r'};t)\right]\right\}} \tag{B2}$$

and

$$U(\boldsymbol{r};t) = -U_0 \sum_{\boldsymbol{r''},\, 0<|\boldsymbol{r'}-\boldsymbol{r}|\leq 3} \frac{\rho(\boldsymbol{r''};t)}{|\boldsymbol{r}-\boldsymbol{r''}|^6}. \tag{B3}$$

We consider a two-dimensional regular lattice of coordination number z and lattice constant a and choose the orthogonal $x-y$ coordinate system such that the $x-$axis is along one of the lattice directions. For a given site $\boldsymbol{r}$ we index the nearest neighbors as $\boldsymbol{r'_j}$, $j = 0, 1, 2, ...z-1$, where $j = 0$ is chosen such that $\boldsymbol{r'_0} - \boldsymbol{r}$ is parallel to the x-axis and j runs in counterclockwise direction. Denoting the angle formed by the vector $\boldsymbol{r'_j} - \boldsymbol{r}$ with the x-axis as ϕ_j so that $\phi_j = 2\pi\frac{j}{z}$, the components x'_j and y'_j of $\boldsymbol{r'_j} - \boldsymbol{r}$ are given by $x'_j = a\cos(\phi_j)$ and $y'_j = a\sin(\phi_j)$. The following relations are satisfied by the angles ϕ_j [60] and will prove to be useful for the rest of the calculation:

$$\sum_{j=0}^{z-1} \sin^k(\phi_j) = 0, \ \sum_{j=0}^{z-1} \cos^k(\phi_j) = 0, \quad k \text{ odd}, 0 < k < z, \tag{B4a}$$

$$\sum_{j=0}^{z-1} \sin^2(\phi_j) = \frac{z}{2}, \ \sum_{j=0}^{z-1} \cos^2(\phi_j) = \frac{z}{2}, \tag{B4b}$$

$$\sum_{j=0}^{z-1} \sin(2\phi_j) = 0, \ \sum_{j=0}^{z-1} \cos(2\phi_j) = 0, \tag{B4c}$$

Defining

$$\delta h(\boldsymbol{r}, \boldsymbol{r'_j}; t) = h(\boldsymbol{r'_j}; t) - h(\boldsymbol{r}; t), \tag{B5}$$

where $h(\boldsymbol{r}; t)$ is any of the functions $\rho(\boldsymbol{r}; t)$, $U(\boldsymbol{r}; t)$, or products of them, expanding $h(\boldsymbol{r'_j}; t)$ near $\boldsymbol{r}$, and sum-

ming $\delta h(\boldsymbol{r},\boldsymbol{r}'_j;t)$ over $\boldsymbol{r}'_j$ one obtains

$$\sum_{j=0}^{z-1}\delta h(\boldsymbol{r},\boldsymbol{r}'_j;t)=a\left[\frac{\partial h}{\partial x}\sum_{j=0}^{z-1}\cos(\phi_j)+\frac{\partial h}{\partial y}\sum_{j=0}^{z-1}\sin(\phi_j)\right]$$
$$+\frac{a^2}{2}\left[\frac{\partial^2 h}{\partial x^2}\sum_{j=0}^{z-1}\cos^2(\phi_j)+2\frac{\partial^2 h}{\partial x\partial y}\sum_{j=0}^{z-1}\sin(\phi_j)\cos(\phi_j)\right.$$
$$\left.+\frac{\partial^2 h}{\partial y^2}\sum_{j=0}^{z-1}\sin^2(\phi_j)\right]+\dots\ . \tag{B6}$$

In the relation above, $h\equiv h(\boldsymbol{r};t)$ and the derivatives are evaluated at $\boldsymbol{r}$. Replacing the corresponding sums by the results in Eq. (B4), it follows that

$$\sum_{j=0}^{z-1}\delta h(\boldsymbol{r},\boldsymbol{r}'_j;t)=\frac{za^2}{4}\nabla^2 h+\mathcal{O}(a^4). \tag{B7}$$

Straightforward algebra allows one to derive from the definition (B5) the following additional useful relations involving a second function $f(\boldsymbol{r};t)$:

$$f(\boldsymbol{r}'_j;t)\delta h(\boldsymbol{r},\boldsymbol{r}'_j;t)=\delta(fh)(\boldsymbol{r},\boldsymbol{r}'_j;t)$$
$$-h(\boldsymbol{r}_j;t)\delta f(\boldsymbol{r},\boldsymbol{r}'_j;t) \tag{B8a}$$
$$\delta f(\boldsymbol{r},\boldsymbol{r}'_j;t)\delta h(\boldsymbol{r},\boldsymbol{r}'_j;t)=\delta(fh)(\boldsymbol{r},\boldsymbol{r}'_j;t)$$
$$-h(\boldsymbol{r}_j;t)\delta f(\boldsymbol{r},\boldsymbol{r}'_j;t)-f(\boldsymbol{r}_j;t)\delta h(\boldsymbol{r},\boldsymbol{r}'_j;t). \tag{B8b}$$

Assuming that $U(\boldsymbol{r};t)$ varies slowly on the scale of the lattice constant so that $\beta\delta U(\boldsymbol{r},\boldsymbol{r}';t)\ll 1$, one has the expansion

$$\frac{\exp\left[-\frac{\beta}{2}\,\delta U(\boldsymbol{r},\boldsymbol{r}'_k;t)\right]}{\sum_{j=0}^{z-1}\exp\left[-\frac{\beta}{2}\,\delta U(\boldsymbol{r},\boldsymbol{r}'_j;t)\right]}\simeq$$
$$\simeq\frac{\exp\left[-\frac{\beta}{2}\,\delta U(\boldsymbol{r},\boldsymbol{r}'_k;t)\right]}{\sum_{j=0}^{z-1}\left\{1-\beta\,\delta U(\boldsymbol{r},\boldsymbol{r}'_j;t)/2+\left[\beta\,\delta U(\boldsymbol{r},\boldsymbol{r}'_j;t)/2\right]^2+\dots\right\}}. \tag{B9}$$

Thus using Eqs. (B7) and (B8b) one obtains

$$\frac{\omega_{\boldsymbol{r}\to\boldsymbol{r}';t}}{\Omega}\simeq\frac{1}{z}\exp\left[-\frac{\beta}{2}\,\delta U(\boldsymbol{r},\boldsymbol{r}'_k;t)\right]\times$$
$$\times\left\{1+\frac{\beta a^2}{8}\,\left[\nabla^2 U-\beta(\nabla U)^2\right]+\mathcal{O}(a^4)\right\}, \tag{B10}$$

where as before $U\equiv U(\boldsymbol{r};t)$ and the spatial derivatives are evaluated at $\boldsymbol{r}$. As we shall show below, the zeroth-order term in the above expansion (Eq. (B10)) contributes to the master equation already in the order a^2, and therefore the other terms on the RHS of Eq. (B10) will lead to contributions proportional to a^4 and higher orders. Therefore, up to contributions which are of second order in the lattice constant in the master equation, Eq. (B10) may be rewritten as

$$\omega_{\boldsymbol{r}\to\boldsymbol{r}';t}\simeq\frac{\Omega}{z}\exp\left[-\frac{\beta}{2}\,\delta U(\boldsymbol{r},\boldsymbol{r}';t)\right]. \tag{B11}$$

This means that the deviations of the rates $\omega_{\boldsymbol{r}\to\boldsymbol{r}';t}$ from detailed balance, which according to Eq. (B10) are of second order and higher in the lattice constant, in the equation corresponding to the continuum limit contribute with terms of fourth order and higher in the lattice constant. These terms become negligible in the limit $a\to 0$.

The expression (B11) may be now expanded in terms of powers of $\beta\delta U(\boldsymbol{r},\boldsymbol{r}';t)$:

$$\omega_{\boldsymbol{r}\to\boldsymbol{r}';t}\simeq p_0+p_1+p_2+\dots\ , \tag{B12}$$

where

$$p_0 = \frac{\Omega}{z}, \tag{B13a}$$
$$p_1 = -\frac{\Omega\beta}{2z}\,\delta U(\boldsymbol{r},\boldsymbol{r}';t), \tag{B13b}$$
$$p_2 = \frac{\Omega\beta^2}{4z}\,[\delta U(\boldsymbol{r},\boldsymbol{r}';t)]^2. \tag{B13c}$$

Note that the expression (B11) implies

$$\omega_{\boldsymbol{r}'\to\boldsymbol{r};t} \simeq \frac{\Omega}{z}\exp\left[-\frac{\beta}{2}\,\delta U(\boldsymbol{r}',\boldsymbol{r};t)\right]$$
$$= \frac{\Omega}{z}\exp\left[+\frac{\beta}{2}\,\delta U(\boldsymbol{r},\boldsymbol{r}';t)\right] \tag{B14}$$

and thus its expansion in powers of $\beta\delta U(\boldsymbol{r},\boldsymbol{r}';t)$ is

$$\omega_{\boldsymbol{r}'\to\boldsymbol{r};t}\simeq p_0-p_1+p_2+\dots\ . \tag{B15}$$

We now will compute separately the contributions of these terms to the RHS of Eq. (B1). For the contribution due to p_0 one has

$$\mathrm{RHS}_{(0)} = \frac{\Omega}{z}\sum_{j=0}^{z-1}\left\{\rho(\boldsymbol{r}'_j,t)[1-\rho(\boldsymbol{r},t)]\right.$$
$$-\left.\rho(\boldsymbol{r},t)[1-\rho(\boldsymbol{r}'_j,t)]\right\}$$
$$= \frac{\Omega}{z}\sum_{j=0}^{z-1}\delta\rho(\boldsymbol{r},\boldsymbol{r}'_j;t)$$
$$= \frac{\Omega a^2}{4}\nabla^2\rho+\Omega\,\mathcal{O}(a^4)\,. \tag{B16}$$

For p_1 one has

$$\begin{aligned}\mathrm{RHS}_{(1)} &= \frac{\beta\Omega}{2z}\sum_{j=0}^{z-1}\delta U(\boldsymbol{r},\boldsymbol{r}'_j;t)\left\{\rho(\boldsymbol{r}'_j,t)[1-\rho(\boldsymbol{r},t)]\right.\\ &+ \left.\rho(\boldsymbol{r},t)[1-\rho(\boldsymbol{r}'_j,t)]\right\}\\ &= \frac{\beta\Omega}{2z}\left[1-2\rho(\boldsymbol{r};t)\right]\sum_{j=0}^{z-1}\rho(\boldsymbol{r}'_j;t)\delta U(\boldsymbol{r},\boldsymbol{r}'_j;t)\\ &+ \frac{\beta\Omega}{2z}\,\rho(\boldsymbol{r};t)\sum_{j=0}^{z-1}\delta U(\boldsymbol{r},\boldsymbol{r}'_j;t). \qquad \text{(B17)}\end{aligned}$$

Using Eqs. (B7) and (B8a) to replace the two sums in the expression above, one obtains

$$\begin{aligned}\mathrm{RHS}_{(1)} &= \frac{\beta\Omega a^2}{8}\left\{(1-2\rho)[\nabla^2(\rho U)-U\nabla^2\rho]+\rho\nabla^2 U\right\}\\ &+\Omega\mathcal{O}(a^4) = \frac{\beta\Omega a^2}{4}\,\nabla[\rho(1-\rho)\nabla U]+\Omega\mathcal{O}(a^4)\,. \qquad \text{(B18)}\end{aligned}$$

Finally, for p_2 one has

$$\begin{aligned}\mathrm{RHS}_{(2)} &= \frac{\beta^2\Omega}{4z}\sum_{j=0}^{z-1}[\delta U(\boldsymbol{r},\boldsymbol{r}'_j;t)]^2\left\{\rho(\boldsymbol{r}'_j,t)[1-\rho(\boldsymbol{r},t)]\right.\\ &- \left.\rho(\boldsymbol{r},t)[1-\rho(\boldsymbol{r}'_j,t)]\right\}\\ &= \frac{\beta^2\Omega}{4z}\sum_{j=0}^{z-1}[\delta U(\boldsymbol{r},\boldsymbol{r}'_j;t)]^2\delta\rho(\boldsymbol{r},\boldsymbol{r}'_j;t)\,. \qquad \text{(B19)}\end{aligned}$$

Using repeatedly Eqs. (B8a) and (B7) in the above sum, one obtains

$$\begin{aligned}\mathrm{RHS}_{(2)} &= \frac{\beta^2\Omega a^2}{4}\left[\nabla^2(\rho U^2)-\rho\nabla^2U^2-U^2\nabla^2\rho\right.\\ &- \left.2U\nabla^2(\rho U)+2U\rho\nabla^2U+2U^2\nabla^2\rho\right]\\ &+ \Omega\mathcal{O}(a^4)=\Omega\mathcal{O}(a^4)\,. \qquad \text{(B20)}\end{aligned}$$

It is easy to see that higher order terms, $p_3,\ldots,$ will contribute with terms which are at least of the order a^4, and thus the expressions (B16) and (B18) are the only terms relevant for Eq. (B1).

Collecting the terms and passing to the continuum limit $a\to 0$, $\Omega^{-1}\to 0$ such that $D_0=\Omega a^2/4$ stays finite, one arrives at the result given in Eq. (13) in the main text, i.e.,

$$\partial_t\rho = D_0\nabla\{\nabla\rho+\beta\left[\rho(1-\rho)\nabla U\right]\}+\mathcal{O}(a^2)\,. \qquad \text{(B21)}$$

APPENDIX C: DERIVATION OF THE SHOCK SOLUTION

Following Ref. [57], we start from equation Eq. (26) written in terms of the scaling variable λ as

$$-\frac{1}{2}\lambda\frac{dC}{d\lambda}=\frac{d^2}{d\lambda^2}\mu(C)+\left(\frac{a}{\sqrt{\tau}}\right)^2 Q\left[\frac{d^4C}{d\lambda^4},\left(\frac{d^2C}{d\lambda^2}\right)^2,\ldots\right], \qquad \text{(C1)}$$

where the function Q is a linear combination of fourth-order derivatives terms of the form $\frac{d^4C}{d\lambda^4}$, $\left(\frac{d^2C}{d\lambda^2}\right)^2$, $\left[\frac{d^2(UC)}{d\lambda^2}\right]^2,\ldots$. The region of interest, $\lambda\in[0,A]$, naturally decomposes into the region near the interface, $\lambda_s-h(\epsilon)\le\lambda\le\lambda_s+h(\epsilon)$, and the outer region $|\lambda-\lambda_s|>h(\epsilon)$ with $\epsilon=a/\sqrt{\tau}$; $h(\epsilon)$ is a smooth function such that $h(\epsilon\to 0)=0$ (which ensures that in the long-time limit the width of the interface becomes negligible) and $\lim_{\epsilon\to 0}\frac{h(\epsilon)}{\epsilon}\to\infty$, i.e., it is assumed that the decrease of the width is slower than ϵ. In the outer region, the solution $C_{l,r}(\lambda)$ is a slowly varying, smooth function of λ, and the terms proportional to ϵ^2 in Eq. (C1) are negligible. In contrast, in the inner region the gradients are very large, and the fourth-order terms become relevant.

In order to obtain the shock structure, we change to the "stretching" variable $\zeta=(\lambda-\lambda_s)/\epsilon$ for $|\lambda-\lambda_s|\le h(\epsilon)$ and look for a smooth, strictly decreasing solution $C(\zeta)$. In terms of ζ Eq. (26) turns into

$$\begin{aligned}&-\frac{1}{2}(\lambda_s+\zeta\epsilon)\epsilon^{-1}\frac{dC}{d\zeta}=\\ &\epsilon^{-2}\frac{d^2}{d\zeta^2}\mu(C)+\epsilon^{-2}Q\left[\frac{d^4C}{d\zeta^4},\left(\frac{d^2C}{d\zeta^2}\right)^2,\ldots\right],\end{aligned} \qquad \text{(C2)}$$

which in the limit $\epsilon\to 0$ leads to the zeroth order in the ϵ-approximation:

$$\frac{d^2}{d\zeta^2}\mu(C)+Q\left[\frac{d^4C}{d\zeta^4},\left(\frac{d^2C}{d\zeta^2}\right)^2,\ldots\right]=0. \qquad \text{(C3)}$$

Since in the limit $\epsilon\to 0$ the inner region $-h(\epsilon)/\epsilon\le\zeta\le h(\epsilon)/\epsilon$ is mapped into $-\infty<\zeta<+\infty$ and at the ends of the shock region the inner solution must match the outer solution $C_{l,r}(\lambda)$, Eq. (C3) should be solved subject to the boundary conditions

$$\lim_{\zeta\to-\infty}C(\zeta)=C_M\ ,\ \lim_{\zeta\to+\infty}C(\zeta)=C_m, \qquad \text{(C4)}$$

which implies also that all the derivatives $C^{(k)}(\zeta)$ of the smooth inner solution $C(\zeta)$ tend to zero as $\zeta\to\pm\infty$.

Although the function Q may be computed explicitly by using Eq. (B7),

$$\sum_{j=0}^{z-1}\delta h(\boldsymbol{r},\boldsymbol{r}'_j;t)=\frac{za^2}{4}\nabla^2h+\frac{3za^4}{8}\nabla^4h+\mathcal{O}(a^6), \qquad \text{(C5)}$$

and following similar steps as in calculating the terms proportional to a^2 in Appendix B, the result is very complicated and a singular perturbation analysis appears to be extremely difficult, if at all possible. However, one may argue that the term $\partial_x^4 C$ is always relevant in the region of the shock because it is associated with an interface contribution $\mathcal{F}_i = \int dx[\nabla C(x,t)]^2$ to the free energy functional $\mathcal{F} = \mathcal{F}_i + \cdots$ of a dynamical Cahn-Hillard theory of phase separation, $\partial_t C = \nabla\left[M(C)\nabla\left(\frac{\delta\mathcal{F}}{\delta C}\right)\right]$ (where $M(C)$ denotes the mobility)[58]. Therefore, all the other terms that are relevant should be of the same order as $\partial_x^4 C$. This leads us to the approximation

$$Q\left[\frac{d^4C}{d\zeta^4}, \left(\frac{d^2C}{d\zeta^2}\right)^2, \dots\right] \simeq q\frac{d^4C}{d\zeta^4}, \tag{C6}$$

with q a constant or a very slowly varying function of λ, e.g., $q(\zeta) = \tilde{q}(\lambda_s + \epsilon\zeta)$. In this case, Eq. (C3) reduces to

$$\frac{d^2}{d\zeta^2}\left[\mu(C) + q\frac{d^2C}{d\zeta^2}\right] = 0. \tag{C7}$$

A first integration leads to $\frac{d}{d\zeta}\left[\mu(C) + q\frac{d^2C}{d\zeta^2}\right] = const = 0$ because both $\frac{d}{d\zeta}\mu(C)$ and $\frac{d^3C}{d\zeta^3}$ are zero at $\zeta \to \pm\infty$, and thus a second integration yields

$$\mu(C) + q\frac{d^2C}{d\zeta^2} = b, \tag{C8}$$

where b is an integration constant. Since $\lim_{\zeta\to\pm\infty}\frac{d^2C}{d\zeta^2} = 0$, one obtains $\mu[C(\zeta \to \pm\infty)] = b$, i.e., the requirement of continuity of $\mu(C)$ across the shock (Eq. (29a) in the main text):

$$\mu(C_M) = \mu(C_m)\ . \tag{C9}$$

Since $\frac{dC}{d\zeta} \neq 0$ (except at infinity) and $b = \mu(C_M)$, Eq. (C8) may be rewritten in the form

$$\frac{q}{2}\frac{d}{d\zeta}\left[\left(\frac{dC}{d\zeta}\right)^2\right] = [\mu(C_M) - \mu(C)]\frac{dC}{d\zeta}\ , \tag{C10}$$

which leads to

$$\int_{C_m}^{C_M} dC[\mu(C_M) - \mu(C)] = \frac{q}{2}\int_{+\infty}^{-\infty} d\zeta\frac{d}{d\zeta}\left[\left(\frac{dC}{d\zeta}\right)^2\right] = 0\ , \tag{C11}$$

i.e., the equal area-rule for $\mu(C)$ (Eq. (29b) in the main text).

Finally, we remark that all the details of the calculation, as well as the main results (Eqs. (C9) and (C11)), remain unchanged if the corrections Q would have the form $Q[C^{(4)}, (C^{(2)})^2, \dots] = \frac{d^2}{d\zeta^2}P[C, C^{(2)}, (C^{(1)})^2, \dots]$, with P a linear combination of terms of second order spatial derivatives satisfying $\lim_{\zeta\to\pm\infty} P \to 0$ [61], and thus it seems reasonable to assume that in general it is *only* the inner structure of the shock that depends on the particular form of Q [57, 58].

[1] S.F. Burlatsky, G. Oshanin, A.M. Cazabat, and M. Moreau, Phys. Rev. Lett. **76**, 86 (1996).
[2] G. Oshanin, J. De Coninck, A.M. Cazabat, and M. Moreau, J. Mol. Liquids **76**, 195 (1998).
[3] P.G. de Gennes, Rev. Mod. Phys. **57**, 827 (1985).
[4] L. Leger and J.F. Joanny, Rep. Prog. Phys. **72**, 431 (1992).
[5] A. Oron, S.H. Davis, and S.G. Bankoff, Rev. Mod. Phys. **69**, 931 (1997).
[6] S. Dietrich, in *NATO-ASI Proceedings: New Approaches to Old and New Problems in Liquid State Theory – Inhomogeneities and Phase Separation in Simple, Complex and Quantum Fluids*, edited by C. Caccamo, J.P. Hansen, and G. Stell (Kluwer, Dordrecht, 1999), Vol. C 529, p. 197.
[7] M. Voué and J. de Coninck, Acta mater. **48**, 4405 (2000).
[8] P. Mitchell, Nature Biotechnology **19**, 717 (2001).
[9] H.A. Stone and S. Kim, AIChE J. **47**, 1250 (2001).
[10] S.W.P. Turner, M. Cabodi, and H.G. Craighead, Phys. Rev. Lett. **88**, 128103 (2002).
[11] D. Lindner, Mat. Res. Soc. Bulletin **26**, 333 (2001).
[12] B. Zhao, J.S. Moore, and D.J. Beebe, Science **291**, 1023 (2001).
[13] B. Zhao, J.S. Moore, and D.J. Beebe, Anal. Chem. **74**, 4259 (2002).
[14] H.W. Hardy, Phil. Mag. **38**, 49 (1919).
[15] F. Heslot, A.M. Cazabat, and N. Fraysse, J. Phys.: Condens. Matter **1**, 5794 (1989).
[16] F. Heslot, A.M. Cazabat, and P. Levinson, Phys. Rev. Lett. **62**, 1286 (1989).
[17] F. Heslot, A.M. Cazabat, P. Levinson, and N. Fraysse, Phys. Rev. Lett. **65**, 599 (1990).
[18] J. Daillant, J.J. Benattar, and L. Leger, Phys. Rev. A **41**, 1963 (1990).
[19] U. Albrecht, A. Otto, and P. Leiderer, Phys. Rev. Lett. **68**, 3192 (1992).
[20] N. Fraysse, M.P. Valignat, F. Heslot, A.M. Cazabat, F. Heslot, and P. Levinson, J. Colloid Interface Sci. **158**, 27 (1993).
[21] M. Voué, M.P. Valignat, G. Oshanin, A.M. Cazabat, and J. De Coninck, Langmuir **14**, 5951 (1998).
[22] E. Pérez, E. Schäffer, and U. Steiner, J. Colloid Interface Sci. **234**, 178 (2001).
[23] P.G. de Gennes and A.M. Cazabat, C. R. Acad. Sci. **310 II**, 1601 (1990).
[24] D.B. Abraham, P. Collet, J. De Conninck, and F. Dunlop, Phys. Rev. Lett. **65**, 195 (1990).
[25] A. Lukkarinen, K. Kaski, and D.B. Abraham, Phys. Rev. E **51**, 2199 (1995).
[26] D.B. Abraham, R. Cuerno, and E. Moro, Phys. Rev. Lett.

88, 206101 (2002).
[27] J. Heiniö, K. Kaski, and D.B. Abraham, Phys. Rev. B **45**, 4409 (1992).
[28] J.A. Nieminen and T. Ala-Nissila, Phys. Rev. E **49**, 4428 (1994).
[29] U. D'Ortona, J. De Coninck, J. Koplik, and J.R. Banavar, Phys. Rev. E **53**, 562 (1996).
[30] M. Haataja, J.A. Nieminen, and T. Ala-Nissila, Phys. Rev. E **53**, 5111 (1996).
[31] T. Ala-Nissila, S. Herminghaus, T. Hjelt, and P. Leiderer, Phys. Rev. Lett. **76**, 4003 (1996).
[32] J. De Coninck, Colloids Surf. A **114**, 155 (1996).
[33] S. Bekink, S. Karaborni, G. Verbist, and K. Esselink, Phys. Rev. Lett. **76**, 3766 (1996).
[34] D.R. Heine, G.S. Grest, and E.B. Webb III, preprint cond-mat/0308165 (2003).
[35] B.W. Cherry and C.M. Holmes, J. Colloid and Interf. Sci. **29**, 174 (1969).
[36] T.D. Blake and J.M. Haynes, J. Colloid and Interf. Sci. **30**, 421 (1969).
[37] A.M. Lacasta, J.M. Sancho, F. Sagues, and G. Oshanin, in *Mat. Res. Soc. Proc.*, Vol. 651, p. T9.1 (2001).
[38] P. Hänggi, P. Talkner, and M. Borkovec, Rev. Mod. Phys. **62**, 251 (1990).
[39] see, e.g., B. Lewis and J.C. Anderson, *Nucleation and Growth of Thin Films* (Academic, New York, 1978).
[40] T.M. Liggett, *Interacting Particle Systems* (Springer, Berlin, 1985).
[41] K. Binder, in *Monte Carlo Methods in Statistical Physics*, edited by K. Binder (Springer, Berlin, 1986), p. 1.
[42] A.P.J. Jansen, preprint cond-mat/0303028 (2003).
[43] E. Adam, L. Billard, and F. Lançon, Phys. Rev. E **59**, 1212 (1999).
[44] P. Neogi, J. Chem. Phys. **105**, 8909 (1996).
[45] G. Oshanin, J. De Coninck, A.M. Cazabat, and M. Moreau, Phys. Rev. E **58**, R20 (1998).
[46] K.-t. Leung, Phys. Rev. E **63**, 016102 (2000).
[47] G. Giacomin and J.L. Lebowitz, Phys. Rev. Lett. **76**, 1094 (1996).
[48] G. Giacomin, J.L. Lebowitz, and E. Presutti, in *Mathematical Surveys and Monographs*, edited by R. Carmos and B. Rozovskii (American Mathematical Society, Providence, 1998), Vol. 64, p. 107.
[49] G. Giacomin, J.L. Lebowitz, and R. Marra, Nonlinearity **13**, 2143 (2000).
[50] M. Hildebrand and A.S. Mikhailov, J. Phys. Chem. **100**, 19089 (1996).
[51] D.G. Vlachos and M.A. Katsoulakis, Phys. Rev. Lett. **85**, 3898 (2000).
[52] R. Lam, T. Basak, D.G. Vlachos, and M.A. Katsoulakis, J. Chem. Phys. **115**, 11278 (2001).
[53] C.M. Elliott and D.A. French, IMA J. Appl. Math. **38**, 97 (1987).
[54] In Ref. [1] the solution $\tilde{C}_{mf}(\lambda)$ is expressed in terms of the parameter μ representing the ratio of the *fixed* probabilities for forward and backward jumping of a particle belonging to the advancing edge of the monolayer. The connection with the expression listed in the main text is made by noting that in the long-time limit the relation $\mu = 1 - C_1$ holds (see Eq. (23b)).
[55] J. Moon, J. Lowekamp, P. Wynblatt, S. Garoff, and R.M. Sutter, Surf. Sci. **488**, 73 (2001).
[56] J. Moon, J. Yoon, P. Wynblatt, S. Garoff, and R.M. Sutter, Comp. Mat. Sci. **25**, 503 (2002).
[57] T.P. Witelski, Appl. Math. Lett. **8**, 27 (1995).
[58] T.P. Witelski, Studies in Appl. Math. **96**, 277 (1996).
[59] G. Wiegand, T. Jaworek, G. Wegner, and E. Sackmann, J. Colloid and Interf. Sci. **196**, 299 (1997).
[60] see, e.g., I.S. Gradshteyn and I.M. Ryzhik, *Table of Integrals, Series, and Products* (Academic, San Diego, 2000), Ch. 1.35.
[61] In this case, Eq. (C11) follows from an integration by parts:

$$\left|\int_{C_m}^{C_M} dC[\mu(C_M)-\mu(C)]\right| = \left|\int_{+\infty}^{-\infty} d\zeta P(\zeta)\frac{dC}{d\zeta}\right|$$
$$\leq \left|C(\zeta)P(\zeta)\Big|_{+\infty}^{-\infty}\right| + \left|\int_{+\infty}^{-\infty} d\zeta C(\zeta)\frac{dP}{d\zeta}\right|$$
$$\leq C_M\left|\int_{+\infty}^{-\infty} d\zeta\frac{dP}{d\zeta}\right| = 0\,.$$